1   **Anatomy of the Indian Summer Monsoon and ENSO**

2   **relationships in state-of-the-art CGCMs:**

3   **Role of the tropical Indian Ocean**

4

5   Pascal Terray[1], KP Sooraj[2], Sébastien Masson[1], Chloé Prodhomme[3]

6

7   **[1] LOCEAN/IPSL, Sorbonne Universités (UPMC, Univ Paris 06)-CNRS-IRD-MNHN, Paris, France**

8   **[2]CCCR, Indian Institute of Tropical Meteorology, Ministery of Earth Sciences, Pune, India**

9   **[3]UB, Departament de fisica fonamental, University of Barcelona, Barcelona, Spain**

10

11

12

13   Revised for **Climate Dynamics**

14   **19 August 2020**

15

16

17

18

19

20

21   **1**

Corresponding author address: Pascal Terray, LOCEAN-IPSL, Sorbonne Universités (Campus Université Pierre et Marie Curie), BP100 – 4 place Jussieu, 75252 Paris cedex 05, France. Tel : +33 1 44 27 70 72. E-mail : terray@locean-ipsl.upmc.fr

Abstract

Indian Summer Monsoon (ISM) rainfall and El Niño-Southern Oscillation (ENSO) exhibit an inverse relationship during boreal summer, which is one of the roots of ISM interannual variability and its seasonal predictability. Here we document how current climate and seasonal prediction models simulate the timing and amplitude of this ISM-ENSO teleconnection. Many Coupled General Circulation Models (CGCMs) do simulate a simultaneous inverse relationship between ENSO and ISM, though with a large spread. However, most of them show significant negative correlations before ISM, which are at odd with observations. Consistent with this systematic error, simulated Niño-3.4 Sea Surface Temperature (SST) variability has erroneous high amplitude during boreal spring and ISM rainfall variability is also too strong during the first part of ISM.

The role of the Indian Ocean (IO) in modulating the ISM-ENSO relationships is further investigated using dedicated experiments with the SINTEX-F2 CGCM. Decoupled tropical Pacific and IO experiments are conducted to assess the direct relationship between ISM and IO SSTs on one hand, and the specific role of IO feedback on ENSO on the other hand. The direct effect of IO SSTs on ISM is weak and insignificant at the interannual time scale in the Pacific decoupled experiment. On the other hand, IO decoupled experiments demonstrate that El Niño shifts rapidly to La Niña when ocean-atmosphere coupling is active in the whole IO or only in its western part. This IO negative feedback is mostly active during the decaying phase of El Niño, which is accompanied by a basin-wide warming in the IO, and significantly modulates the length of ENSO events in our simulations.

This IO feedback operates through a modulation of the Walker circulation over the IO, which strengthens and shifts eastward an anomalous anticyclone centered on the Philippine Sea and associated easterly wind anomalies in the equatorial western Pacific during boreal winter. In turn, these atmospheric anomalies lead to a fast ENSO turnabout via oceanic adjustement processes mediated by eastward propagating upwelling Kelvin waves. An experiment in which only the SouthEast Indian Ocean (SEIO) is decoupled, demonstrates that the equatorial SST gradient in the IO during boreal winter plays a fundamental role in the efficiency of IO feedback. In this experiment, simulated ISM-ENSO lead-lag correlations match closely the observations. This success is associated with removal of erroneous SEIO SST variability during boreal winter in the SEIO decoupled experiment. Finally, it is illustrated that most CMIP5 CGCMs exhibit similar SST errors in the SEIO during boreal winter in addition to an exaggerated SEIO SST variability during boreal fall.

Keywords: Indian Summer Monsoon; El Niño-Southern Oscillation; Indian Ocean; ocean-atmosphere interactions; coupled climate model.

1. Introduction

The climate of South Asia is dominated by the monsoon, which returns with remarkable regularity in each summer and provides the rainfall needed to sustain over 60% of the world's population. The Indian subcontinent is thus strongly dependent on the timing and amount of precipitation falling during the monsoon season (from June through September, JJAS hereafter) and is one of the most vulnerable regions of the world as far as water resources is concerned. Predicting and projecting (for the next century) the Indian Summer Monsoon (ISM) rainfall variability are, thus, both a scientific challenge and a key-societal need.

On inter-annual time scales, the ISM rainfall exhibits the multiyear (3-7 years) El-Niño-Southern-Oscillation (ENSO) frequency (Mooley and Parthasarathy 1983; Webster et al. 1998; Lau and Wang 2006). ENSO is the most dominant form of ocean-atmosphere coupled variability on interannual time scales and affects climate worldwide through atmospheric and oceanic teleconnections (e.g., Tourre and White 1995; Alexander et al. 2002; Clarke 2008; Wang 2019). The effect of ENSO on the ISM has been intensively studied for decades (Walker 1924; Sikka 1980; Keshavamurthy 1982; Webster et al. 1998; Lau and Nath 2000, 2012; Gadgil et al. 2004; Cherchi et al. 2007; Pillai and Anamalai 2012). During El Niños, the Walker circulation shifts eastward, inducing subsidence and dry conditions in the Indian sector and vice-versa during La Niñas (Walker 1924; Sikka 1980; Rasmusson and Carpenter 1983; Webster et al. 1998; Lau and and Nath 2000, 2012). It is therefore extremely important to examine if the ENSO-ISM relationships are well simulated in state-of-the art climate and seasonal forecasting models (Annamalai et al. 2007; Terray et al. 2012; Sperber et al. 2013; Jourdain et al. 2013; Sabeerali et al. 2019; Krishna et al. 2019).

Though the probability of occurrence of a weak (strong) ISM during an El Niño (La Niña) is large, still ENSO can explain only about 35% the interannual variance of ISM rainfall (Krishna Kumar et al. 2006). Moreover, the ISM-ENSO relationship has considerably weakened during some periods (Torrence and Webster 1999), so that it is important to look for other sources of ISM predictability. In addition to ENSO, many studies have pointed out significant connections between ISM and the Indian Ocean (IO) Sea Surface Temperatures (SST) anomalies (Rao and Goswami 1988; Ashok et al. 2001, 2004; Gadgil et al. 2004, 2005, 2007; Krishnan et al. 2003; Terray et al. 2003, 2007; Cherchi et al. 2007; Park et al. 2010; Boschat et al. 2011; Lau and Nath 2012; Cherchi and Navarra 2013; Shukla and Huang 2016). In particular, it has been suggested that the Indian Ocean Dipole (IOD; Saji et al. 1999; Webster et al. 1999) interacts with both ENSO and ISM (Ashok et al. 2001, 2004; Drbohlav

88 et al. 2007; Loschnigg et al. 2003; Schott et al. 2009; Luo et al. 2010; Izumo et al. 2010;

89 Wang 2019). Positive IOD events are associated with cool SST and shallow thermocline in

90 the eastern Indian Ocean (IO), and warm SST and deep thermocline in its western part (Li et

91 al. 2003; Gualdi et al. 2003; Spencer et al. 2005; Fischer et al. 2005; Schott et al. 2009). The

92 way IOD can influence ISM remains controversial. Some authors suggest a direct influence of

93 positive IOD events through moisture transport over the western IO or modifications of the

94 local Hadley cell with increased ascendance over India, both factors enhancing ISM rainfall

95 (Ashok et al. 2001, 2004; Gadgil et al. 2004; Behera et al. 2005; Ashok and Saji 2007). It has

96 also been suggested that IOD counteracts the influence of ENSO on ISM (Ashok et al. 2001,

97 2004; Ashok and Saji 2007; Ummenhofer et al. 2011; Krishnaswamy et al. 2015).

98   More recently, more complex interactions between ISM, IOD and ENSO have been

99 evidenced, adding even more complexity to the emerging picture. It has been suggested that a

100 strong ISM can favor a negative IOD event by producing westerly wind anomalies over the

101 equator IO during boreal fall and that ENSO, ISM and IOD are strongly inter-related

102 components of the Tropospheric Biennial Oscillation (TBO) in the Tropics (Terray 1995;

103 Meehl 1997; Meehl and Arblaster 2002, 2003; Loschnigg et al. 2003; Terray et al. 2003,

104 2005b; Drbohlav et al. 2007; Webster and Hoyos 2010; Li and Hsu 2017). IODs have also

105 been suggested as a potential trigger of ENSO events (Luo et al. 2010; Izumo et al. 2010;

106 Zhou et al. 2015; Jourdain et al. 2016; Wieners et al. 2017ab; Cai et al. 2019). It has been

107 further discovered that the the Indian Ocean Basin (IOB) mode, associated with ENSO-

108 related subsidence during the decaying phase of El Niños (e.g., Klein et al. 1999; Alexander

109 et al. 2002; Xie et al. 2009, 2016; Schott et al. 2009; Wang 2019), provides an important

110 forcing on ISM variability (Yang et al. 2007; 2010; Park et al. 2010; Boschat et al. 2011,

111 2012; Chowdary et al. 2017).

112   Because of the interactive nature of the tropical Indo-Pacific ocean-atmosphere system and

113 the near-global patterns of ISM teleconnections summarized above, one of the best tools to

114 simulate and predict ISM variability is a global Coupled General Circulation Model (CGCM;

115 Wu and Kirtman 2005; Wang et al. 2005; Zhu and Shukla 2013). In order to provide reliable

116 seasonal predictions and climate projections of ISM rainfall, it is nevertheless essential that

117 CGCMs produce a reasonable simulation of the mean summer monsoon circulation and

118 rainfall distribution, as well as its variability at different time scales. Unfortunately, this is still

119 an area under rapid development, and CGCMs are still at a relatively early stage (Shukla et

120 al., 2009). Most current CGCMS exhibit deficiencies in simulating ISM, ENSO and the IO

121 variability (Bollasina and Ming 2013; Levine et al. 2013; Prodhomme et al. 2014, 2015; Li

and Xie 2012, 2014; Li et al. 2015, 2017ac; Ham and Kug 2014; Bellenger et al. 2014; Anamalai et al. 2017; Terray et al. 2018). So far, we have only a poor understanding of the relative roles of local ocean-atmosphere coupling (e.g. IO) and ENSO in the occurrence of extreme ISMs both in observations and coupled simulations (Gadgil et al. 2005; Saha et al. 2016; Krishna et al. 2019). In particular, the way the IOD and IOB modes influence ISM and interact with ENSO remains unclear (Wu and Kirtman 2004ab; Achuthavarier et al. 2012; Li et al. 2015, Annamalai et al. 2017), and may limit drastically ISM seasonal predictability and the accuracy of ISM projections (Sabeerali et al. 2019; Li et al. 2017ac).

Taking into account the large uncertainties in the sign and amplitude of the ENSO-IO-ISM relationships, we will document in this work, (i) the ability of state-of-the-art CGCMs to simulate the ENSO-ISM relationship and (ii) the possible role of the IO (e.g. the IOD and IOB modes) in modulating this relationship. More precisely, we will document errors in the simulation of the ENSO-ISM relationship in CMIP5 and some seasonal forecasting CGCMs and analyze a set of decoupling experiments performed with a global CGCM, the SINTEX-F2 model (Masson et al. 2012), to diagnose the possible origins of these errors. Such decoupling approach has been already successfully used to analyze the role of Indian and Atlantic oceans on ENSO (Ohba and Ueda 2007; Luo et al. 2010; Santoso et al. 2012; Ohba and Watanabe 2012; Terray et al. 2016; Kajtar et al. 2017), the impacts of SST errors on ISM (Prodhomme et al. 2014, 2015), and the IOD evolution and its forcing mechanisms in the absence of ENSO (Fischer et al. 2005; Behera et al. 2005, 2006; Yang et al. 2015; Cretat et al. 2017, 2018; Stuecker et al. 2017; Wang et al. 2016, 2019).

This paper is organized as follows. The coupled models, the sensitivity experiments and validation datasets used in this study are described in Section 2. In Section 3, we document the ISM-ENSO relationships in observations and the errors in simulating these relationships by current CGCMs. In Section 4, we analyze decoupling experiments performed with the SINTEX-F2 CGCM, in which tropical Pacific or IO SST variability is removed, in order to assess the "intrinsic" role of IO SSTs on ISM, ENSO and the ISM-ENSO relationship and to understand their potential roles on the errors in the simulation of the ISM-ENSO relationship. The final section summarizes the main results of the present work and discusses if and how these results apply to CMIP5 models.

2. Observed datasets, coupled models and sensitivity decoupling experiments

2.a Observed datasets

To study ISM variability and its teleconnection with ENSO, we have used three different observed rainfall datasets. Firstly, we considered the extensively used classical All-India-Rainfall (AIR) dataset, based on quality-controlled rain-gauge data, for the period 1870-2012 (Parthasarathy et al., 1994; Krishna Kumar et al. 1999; Bodai et al. 2020). The second rainfall dataset included in our analysis is a high-resolution (e.g. 0.25° x 0.25°) quality-controlled gridded (daily) rainfall dataset, for the period 1901-2013, as obtained from the Indian Meteorological Department (IMD; see Pai et al. 2015 for precise details). Finally, we also used the Global Precipitation Climatology Project rainfall dataset (GPCP at 1° x 1° spatial resolution; Huffman et al. 2001), which combines measures of precipitation gauges and satellite data. GPCP is analysed for the 1979-2012 period. For both IMD and GPCP, the ISM Rainfall (ISMR) time series is defined as the average of rainfall anomalies for the land grid points in the region 5°N to 25°N and 70°E to 95°E.

The Niño-3.4 SST (monthly average of SST anomalies in the region 5°S to 5°N and 170° to 120°W) time series is chosen for the ENSO index since in observations the strongest correlations between ISMR and tropical Pacific SSTs occur over this region (not shown). This is consistent with past studies (Krishna Kumar et al. 2006; Jourdain et al. 2013). However, this practical choice implies that our study mainly focuses on canonical ENSO events rather than on El Niño Modoki events (Ashok et al. 2007). The Niño-3.4 SST time series is estimated from the Hadley Centre Sea Ice and SST dataset (HadISST1.1; Rayner et al. 2003). But similar results (not shown) are obtained with other SST datasets such the ERSST dataset (Huang et al. 2017) or the AVHRR only daily Optimum Interpolation SST version 2 (OISSTv2) dataset (Reynolds et al. 2007).

2.b Climate models

In order to give a complete overview of the capacity of current CGCMs to simulate the ENSO-ISM relationship, we first considered monthly mean outputs from Coupled Model Intercomparison Project Phase 5 (CMIP5) coupled models available at url: http://cmip-pcmdi.llnl.gov/cmip5/data_portal.html (Taylor et al. 2012). We analyzed the twentieth century simulations of 25 CMIP5 models (see Table S1 in Supplementary Materials for list of models) and for all the models we use the first ensemble member (''r1i1p1'' from CMIP5 database) from each model. We also used long free runs of two state-of-the-art global CGCMs, the CFSv2 (Saha et al. 2014) and the SINTEX-F2 (Masson et al. 2012). The lengths of these control simulations are 80 and 210 years, respectively, for the CFSv2 and SINTEX-F2 CGCMs.

The CFSv2 is the CGCM adopted for operational seasonal forecasting in the US by the National Centers for Environmental Prediction (NCEP; Saha et al. 2014) and in India, in the framework of the Monsoon Mission project (Rao et al. 2019). Its atmospheric model, the Global Forecast System (GFS) is run at T126 spectral resolution (about 0.9° by 0.9°) with 64 sigma-pressure hybrid levels. Its oceanic component has a 0.25-0.5° horizontal resolution, 40 vertical levels and includes an ice model. The atmosphere and ocean exchange quantities such as heat and momentum fluxes every half an hour, with no flux adjustment. See Saha et al. (2014) for further details on the CFSv2 model.

The SINTEX-F2 is used by JAMSTEC (e.g. Japan) for operational seasonal forecasting (Luo et al. 2005; Doi et al. 2016). A comprehensive description of SINTEX-F2 can be found in Masson et al. (2012). The atmospheric component is ECHAM5.3 and is run at T106 spectral resolution (about 1.125° by 1.125°) with 31 hybrid sigma-pressure levels (Roeckner et al. 2003). The oceanic component is NEMO (Madec 2008), using the ORCA05 horizontal resolution (0.5°), 31 unevenly spaced vertical levels and including the LIM2 ice model (Timmermann et al. 2005). The coupling information, without any flux corrections, is exchanged every 2 h using the Ocean-Atmosphere-Sea Ice-Soil coupler (Valcke 2006). The performance of the SINTEX-F2 model in simulating the mean state and interannual variability in the Indo-Pacific areas has been assessed many times and is not repeated here (Masson et al. 2012; Terray et al. 2012, 2016, 2018; Prodhomme et al. 2014, 2015; Cretat et al. 2017, 2018).

Note, finally, that the SINTEX-F2 and CFSv2 configurations used here employ fixed CO_2 concentrations corresponding to present day conditions. This is consistent with the use of recent observations (e.g. mostly 1979-2012) for validation of model outputs.

In all simulations, we characterize the ISM by the JJAS average precipitation over India (5°-25°N and 70°-95°E, land only; ISMR index hereafter) and ENSO by the Niño-3.4 box-average SST as in observations.

2.c Partial decoupling experiments

In addition to the 210-year control run described above (named CTRL hereafter), we perform three partial decoupling experiments (named FTPC, FTIC and FSEIC hereafter), where the model SSTs in the tropical Pacific, Indian oceans and SEIO region are, respectively, nudged to a daily SST climatology obtained from CTRL (see Table 1 for details and definition of the acronyms used to design the nudged experiments), as described in Luo et al. (2005) and Appendix. The damping constant used is -2400 W m^{-2} K^{-1}, which corresponds

221   to the 1-day relaxation time for temperature in a 50-m ocean layer. In these experiments there

222   are no significant changes in SST mean state and seasonal cycle in the nudged regions, but

223   also in the whole Tropics compared to CTRL (see Figs. 1b-d and 2), but, SST variability is

224   suppressed in the nudged region (not shown; see Terray et al. 2016 and Cretat et al. 2017 for

225   illustration). The FSEIC experiment is designed to assess the role of the SST SEIO

226   variability, and by extension of the IOD (as the SEIO region almost matches the eastern pole

227   of the traditional IOD index in observations). Furthermore, despite the SST SEIO bias is

228   modest in the annual mean (Fig. 1a), this region is affected by severe seasonally varying SST

229   mean and variability biases in the SINTEX model (Fig. 2; Fischer et al. 2005; Terray et al.

230   2012; Prodhomme et al. 2014; Cretat et al. 2017). The CGCM simulates a too shallower

231   thermocline in the eastern Indian Ocean during boreal summer and fall. The thermocline-

232   surface coupling is thus amplified in the annual cycle with deeper and cooler water easily

233   upwelled at the surface, cooling drastically the SST mean and enhancing the SST variability

234   in the SEIO during boreal summer and fall (Fig. 2). In addition, the SEIO SST is affected by a

235   strong warm mean bias and also a too strong SST variability during late boreal winter in

236   CTRL (Fig. 2). The FSEIC experiment will therefore be useful to understand the specific role

237   of this amplified SST variability in the SEIO during these two critical seasons on the

238   simulated ENSO, ISM and their relationships.

239   Finally, in order to discuss the remote or local origins of these SST errors in the SEIO in

240   Section 5, an additional partial decoupling experiment (named FTPC-obs hereafter) will be

241   considered. This run is similar to the FTPC experiment, excepted for the use of a daily

242   climatology computed from the OISSTv2 dataset for the 1982-2010 period (Reynolds et al.

243   2007) in the nudging procedure (Table 1). In this FTPC-obs run, the large feedback value

244   applied removes the SST mean biases (in CTRL) with respect to the observed SST

245   climatology, in addition of suppressing the SST variability in the restoring tropical Pacific

246   domain (Fig. 1e).

247   Table 1 summarizes the specifications of the different sensitivity experiments used here

248   and the different nudging domains are displayed in Fig.1b-d. Finally, in the analyses

249   described in Sections 3, 4 and 5, the first 10 years of all simulations have been excluded due

250   to the spin-up of the coupled model.

251

3. ISM-ENSO relationships in observations and CGCMs

253   We first document the amplitude and timing of the relationship between ENSO and ISM in

254 observations in order to provide a basis for a fair assessment of the performance of current

255 CGCMs with respect to this metric in the next subsection.

256 3.a Observed ISM-ENSO relationships

257   In order to illustrate this relationship, we computed the lead-lag correlations between the

258 different ISMR time series and the Niño-3.4 SST bimonthly time series in a three years

259 window from the beginning of year -1 to the end of year +1, the year 0 referring to the year of

260 the ISM season (Fig. 3a-b). Correlation coefficients have been estimated with and without

261 detrending of the different rainfall and SST time series in order to assess the robustness of the

262 results with respect to anthropogenic related trends and nonstationarity of the time series.

263 Detrending has been performed with locally weighted regression, a non-parametric method

264 for fitting a smoothed regression curve to data through local smoothing (Cleveland and

265 Devlin 1988). As results are similar, we only show the results from detrended data here.

266   Consistent with the TBO pattern, involving ENSO and ISM (Yasunari 1990; Meehl 1997;

267 Meehl and Arblaster 2002; Loschnigg et al. 2003; Terray et al. 2003, 2005b; Webster and

268 Hoyos 2010), two distant correlation peaks of opposite signs are noted (Fig. 3a-b). Positive

269 correlations are evident one year before the monsoon for most ISMR indices and time

270 periods. Theses significant positive correlations preceding ISM have largely amplified during

271 recent decades, e.g. after the 1976/77 climate shift and have been explained by a delayed

272 ENSO effect on the ISM, mediated by the IOB warming, which follows the strong El Niño

273 events, such as the 1982-83 and 1997-98 events (Yang et al. 2007, 2010; Park et al. 2010;

274 Boschat et al. 2011, 2012. The correlations switch sign around April-May (AM) and become

275 again statistically significant only in June-July (JJ) of year 0 (Webster and Yang 1992;

276 Webster et al. 1998). These negative correlations between Niño-3.4 SSTs and ISMR peak

277 during boreal fall and fade away progressively after, e.g. during the peaking and decaying

278 phases of El Niño (Fig. 3a-b). The significant negative correlation between ISMR and Niño-

279 3.4 SSTs during boreal summer of year 0 implies that warmer (cooler) SSTs over these

280 regions will suppress (enhance) ISM rainfall consistent with the studies summarized in the

281 introduction. This synchronous effect can be termed the "direct" ENSO effect by opposition

282 to the "indirect" effect mediated by the IOB warming induced by ENSO (Wu et al. 2012).

283   Fig. 3a-b also demonstrates that the synchronous correlation between ISM and ENSO is

284 decreasing for more recent (and shorter) time periods. Interestingly, the lead correlations

285 between ENSO of year -1 and ISM follow an opposite evolution. The decreasing synchronous

286 correlation has lead to the suggestion that the ISM-ENSO relationship has weakened during

287 recent decades for reasons which are still a matter of debate (Krishna Kumar et al. 1999,

288 2006; Torrence and Webster 1999; Gershunov et al. 2001; Ashok et al. 2001, 2004, 2007;

289 Kinter et al. 2002; Annamalai et al. 2007; Kucharski et al. 2007, 2008; Chen et al. 2010;

290 Boschat et al. 2012; Li and Ting 2015; Srivastava et al. 2015; Cash et al. 2017; Yun and

291 Timmermann 2018; Feba et al. 2019; Bodai et al. 2020).

292 3.b Simulated ISM-ENSO relationships

293   We first focus on the capacity of the SINTEX-F2 and CFSv2 coupled models to simulate

294 the ISM-ENSO relationship (Fig. 4a). The two CGCMs are able to reproduce the synchronous

295 negative correlation between ISM and ENSO, though with varying amplitude (Fig. 4.a).

296 However, before ISM, the two CGCMs show large discrepancies from observations with

297 negative and significant correlations during an extended period of several months before ISM.

298 In the CFSv2 model, the lead-lag correlations suggest that ISM is linked to ENSO *before ISM*

299 *rather than during and after ISM* since the maximum negative correlation occurring at lag 0,

300 e.g. JJ of year 0. Moreover, after ISM, the negative correlation quickly fades away in

301 disagreement with observations. The SINTEX-F2 performs slightly better, but shares the

302 same deficiency during the pre-onset period.

303   We next examined the lead-lag correlations between the Niño-3.4 SST and ISMR in

304 CMIP5 CGCMs (Fig. 5a). Here, the correlation coefficients are computed from the first

305 member of each model's ensemble of historical runs and for the period 1950-2000. ISM and

306 its relationships to ENSO in CMIP5 models have already been investigated in many studies

307 (Sperber et al. 2013; Terray et al. 2012); Jourdain et al. 2013; Ramu et al. 2018), but most of

308 them focus on the synchronous relationship (e.g. during boreal summer) between the two

309 phenomena. Here we examine the lead-lag relationships between the two phenomena in more

310 details following the same framework as used above for observations, the SINTEX-F2 and

311 CFv2 models, complementing the results of Jourdain et al. (2013).

312   Many CMIP5 CGCMs are able to reproduce the synchronous negative correlation between

313 ISM and ENSO, although in many models the amplitude of this correlation is erroneous and

314 the diversity (e.g. spread) is large between the CGCMs (Figure 5a). However, a striking

315 feature is that almost all of the CMIP5 CGCMs fail to capture the observed lead-lag

316 relationships between ENSO and ISM. In particular, most CGCMs show erroneous large

317 negative correlations before ISM, which are completely absent in observations, and the

318 observed TBO pattern with positive correlations preceding the ISM by nearly one year is

319 lacking in all CMIP5 CGCMs. In a similar fashion, the simulated correlations are much

320   weaker than observed after the boreal summer of year 0.

321   In other words, current CGCMs show large deficiencies in recovering the observed leag-

322   lag relationships between ISM and ENSO, which is of paramount importance for seasonal

323   forecasting (Gadgil et al. 2005) or climate projections of ISM rainfall (Li et al. 2017ac). It is

324   therefore necessary to go a step further in the model validation to analyze more thoroughly

325   the reasons of this deficiency in current CGCMs, which is the goal of the next sections.

326   3.c Simulated ENSO seasonal phase-locking

327   Though considerable improvements in the simulation of ENSO have been made during the

328   past decades, current CGCMs still need to be improved with regard to realistically

329   representing ENSO (Bellenger et al. 2014). As an illustration, the tendency to produce a

330   double intertropical convergence zone in the Pacific basin, a poor representation of the SST

331   annual cycle and mean pattern in the tropical Pacific, and a substantial underestimation of

332   ENSO variability are recurrent biases shared by many past and present CGCMs (AchutaRao

333   and Sperber 2002, 2006; Li and Xie 2012; 2014; Bellenger et al. 2014). Thus, a biased

334   representation of ENSO in the tropical Pacific itself can be a primary plausible reason for an

335   improper simulation of the ISM-ENSO relationship in current CGCMS (Jourdain et al. 2013).

336   However, Indian and Atlantic SSTs can also matter as they have an overall damping effect on

337   ENSO and modulate the length of the ENSO events (Dommenget et al. 2006; Terray et al.

338   2016).

339   The phase locking of ENSO events to the annual cycle, with a tendency to peak at the end

340   of the calendar year, the amplitude and length of El Nino events (e.g. ENSO periodicities) are

341   among the most distinctive characteristics of ENSO (Rasmusson and Carpenter 1983; Clarke

342   2008; Ham and Kug 2014; Li and Hsu 2017). Obviously, the incorrect annual phase-locking

343   of ENSO's variability is a plausible candidate for explaining the current failure of state-of-

344   the-art CGCMs in the simulation of the ISM-ENSO lead-lag relationships, since most coupled

345   models do simulate a boreal summer monsoon over India (Figs. 4d and 5d). In Figures 4b and

346   5b, we show the monthly standard deviations of the Niño-3.4 SST anomalies from

347   observations, the SINTEX-F2, CFSv2 and CMIP5 CGCMs, respectively. Observed ENSO

348   variability typically peaks in boreal winter and diminishes in boreal spring with relatively

349   modest variability in boreal summer and early fall (Fig. 4b), which is related to the fact that El

350   Niño's onset frequently occurs in boreal spring or early boreal summer (Clarke 2008).

351   It is apparent that both the SINTEX-F2 and CFSv2 models have a preference for relatively

352   high SST variability in the Niño-3.4 region during boreal winter, as observed (Fig. 4b).

353   However, the monthly Niño-3.4 SST standard deviations in these models are higher than

354   observed during boreal spring suggesting that ENSO onset is early than observed or that

355   ENSO decay is slower than observed in the CGCMs. This bias is consistent with the lead-lag

356   ISM-ENSO relationships simulated in the two models, especially the unrealistic negative

357   correlations between ISM and the Niño-3.4 SST preceding the ISM onset (Fig. 4b). This is

358   further confirmed by a lead-lag correlation analysis of SSTs with the ISMR index in the

359   SINTEX-F2 model (see Fig. S1a-f or Figures 3 and 5 of Boschat et al. (2012) for similar

360   analysis on observations). Also consistent with these erroneous negative correlations, the ISM

361   rainfall monthly standard deviations are also exaggerated at the beginning of ISM in the

362   simulations (Fig. 4c).

363   On the other hand, many CMIP5 models show a different seasonal Niño-3.4 SST

364   evolution, with the peak of canonical El Niños occurring at any season (Fig. 5b; Ham and

365   Kug 2014; Taschetto et al. 2014) and only a few models have Niño-3.4 SST variability above

366   observations during boreal winter (Fig. 5b). This can be related to many factors, especially

367   spatial shift of simulated SST variability over the equatorial Pacific often associated with the

368   cold tongue bias (Collins et al. 2010; Li and Xie 2014; Swapna et al. 2015). However, most of

369   them also produce a too large and erroneous ENSO variability during boreal spring as the

370   SINTEX-F2 and CFSv2 models (Figs. 4b and 5b). Consistent with this deficiency and the

371   erroneous negative correlations before ISM (Fig. 5a), the simulated ISM rainfall monthly

372   standard deviations are again exaggerated at the beginning of ISM in most CMIP5 models

373   (Fig. 5c). This exaggerated simulated ENSO variability during boreal spring and early

374   summer can be due to (i) ENSO onsets occurring earlier in the CGCMs, (ii) ENSO events

375   lasting longer with an extended maturing phase compared to observations, or both.

376   While SST mean biases, ENSO pattern or position of peak and deficient ENSO

377   teleconnections may also modulate ISM-ENSO relationships in CGCMs (Jourdain et al.

378   2013), we will show in the next section that length and seasonal phase-locking of ENSO

379   events are key-factors for a realistic simulation of the lead-lag ISM-ENSO relationships.

380

381   **4. Indian Ocean impacts on the ENSO-ISM relationship in the SINTEX-F2 CGCM**

382   To disentangle the role of IO SST variability in shaping the ISM-ENSO relationships, we

383   now analyzed decoupling experiments performed with SINTEX-F2 (see Section 2c).

384   4.a Intrinsic ISM teleconnections

385   We first investigate the possible "intrinsic" role of SST anomalies outside of the tropical

386   Pacific on the ISM, as an important factor in shaping the ENSO-ISM relationship. The

387   analysis is done with the help of the FTPC simulation, where ENSO is removed. By contrast,

388   in the next subsection, we will investigate the possible role of IO SST anomalies on ENSO

389   itself, as a second factor in shaping the simulated ENSO-ISM relationship with the help of the

390   other sensitivity experiments in which the tropical IO SST variability, or parts of it, is

391   suppressed.

392   Figure 6.a-d displays the regressions of the JJ and August-September (AS) 850-hPa wind

393   and rainfall fields onto the ISMR index for CTRL and FTPC. As expected, Fig. 6.a-d show

394   enhanced rainfall over India and the neighboring oceanic regions, as well as a strengthening

395   of both the monsoon low-level winds over the Arabian Sea and the Somali jet along the

396   African coast. Next, ISM rainfall anomalies are very sensitive to the perturbation of the

397   Walker circulation that is characteristic of La Niña/El Niño episodes in CTRL (Fig. 6.a-b).

398   Positive rainfall anomalies develop over the maritime continent and neighboring ocean areas

399   and a negative IOD like rainfall pattern emerged over the equatorial IO during AS of strong

400   ISMs and La Niña episodes, consistent with previous works (Webster et al. 1998; Lau and

401   Nath 2000, 2003, 2012; Cretat et al. 2017).

402   By contrast, in FTPC, the atmospheric response associated with the strong/weak ISMs is

403   mostly confined northward of 10°N and is characterized by an anomalous rainfall pattern

404   opposing India and the northwest Pacific region (Fig. 6c-d; Terray et al. 2005a; Wang 2006;

405   Gu et al. 2010; Kosaka et al. 2013; Cretat et al. 2017). Interestingly, ISMR rainfall standard

406   deviations are only slightly reduced (at most of 0.2 mm/day, see Fig. 8c) in FTPC. This result

407   may seem contradictory with the expectation that ENSO is the main driver for ISM

408   interannual variability, but is consistent with the large internal variability associated with ISM

409   and the fact that ISM is also an active player in tropical climate (Yasunari 1999; Kirtman and

410   Shukla 2000). Further, boreal summer rainfall and wind anomalies are very weak outside this

411   north Indo-Pacific region, especially over the equatorial IO.

412   We now examine the extent to which SST forcing outside the tropical Pacific may explain

413   ISM rainfall variability in the absence of ENSO. This is done through a lead-lag correlation

414   analysis between the ISMR index and bi-monthly SST and 200-hPa velocity potential

415   anomalies in the CTRL and FTPC experiments (Figs. S1 and 7). Correlations between ISMR

416   and SSTs in CTRL confirm the existence of a significant statistical association between ISM,

417   ENSO and IOD (Fig. S1a-f), as discussed in the Introduction. Some significant correlations

418   are also seen in the extratropical Pacific and the tropical Atlantic during boreal summer and

13

winter (Fig. S1c-f), which are also consistent with well-known ENSO teleconnections (Wang 2019). On the other hand, correlations between ISMR and SSTs are strikingly different in FTPC (Fig. 7a-f). They are weak before, during and after ISM, except for a significant cooling (warming) of the Arabian Sea (the south of the bay of Bengal) during boreal summer (Fig. 7a-f). This local response is fully consistent with a "slave ocean scenario" in which the SST is mainly controlled by evaporative cooling and local upwelling associated with the strengthening of the monsoon low-level winds and the sea-saw between ISM and the northwest Pacific monsoon discussed above (see Fig. 6c-d). Moreover, simulated ISM variability is not significantly associated with SST anomalies or modulations of the Walker cell over the equatorial IO during boreal summer and fall (Fig. 7c-e and i-k) despite the fact that IODs do exist in the absence of ENSO in FTPC (Fig. 2b; Cretat et al. 2017, 2018). These results invalidate the hypothesis that the direct impact of IOD on ISM may induce a significant modulation of the ENSO-ISM relationship in SINTEX-F2.

On the other hand, the results in CTRL (Fig. S1) are fully consistent with a scenario in which ENSO, ISM and IOD are strongly inter-related components of the TBO in the Tropics (Meehl and Arblaster 2002, 2003; Drbohlav et al. 2007; Webster and Hoyos 2010) since a strong ISM is significantly correlated with La Niña and a negative IOD in CTRL (Fig. 6a-b and S1). However, the FTPC experiment demonstrates that this ENSO-ISM-IOD coupling is mainly due to the ENSO forcing on both ISM and the equatorial IO separately, and not to a direct association between ISM and the equatorial IO, at least in this CGCM.

Furthermore, the 200-hPa velocity potential anomalous patterns associated with ISMR variability confirm the hypothesis that ISM is an active player for the whole tropical circulation in the absence of ENSO. The only physically consistent anomalous 200-hPa velocity potential pattern emerging in Fig. 7g-l is the strong upper-level divergence flow associated with ISM itself and the induced significant strengthening of the subtropical anticyclones over the Pacific and South Atlantic (Fig. 7i-j). Thus, the upper-level circulation anomalies during boreal summer in FTPC are dominated by an enhancement of the zonal monsoon cyclone-subtropical anticyclone circulation driven by the east-west differential heating (Rodwell and Hoskins 2001; Chen 2003). On the other hand, in CTRL, the 200-hPa velocity potential correlation pattern (Fig. S1g-l) has a more large-scale structure and is tightly and significantly linked to ENSO evolution (Fig. S1a-f), as expected (Webster et al. 1998).

In summary, the results of this section strongly suggest that direct (e.g. when ENSO is removed) effects of interannual SST anomalies outside of the tropical Pacific on ISM are

14

weak and do not play a direct role in shaping the ENSO-ISM relationship in the SINTEX-F2 model.

4.b Indian Ocean impacts on ENSO

However, the tropical IO can also influence the ENSO-ISM relationship by directly modulating ENSO in the tropical Pacific itself. Many studies have also highlighted the strong impact of the IOB in accelerating the El Niño to La Niña transition in the tropical Pacific (Kug and Kang 2006; Dommenget et al. 2006; Ohba and Ueda 2007; Jansen et al. 2009; Okumura et al. 2011; Ohba and Watanbe 2012; Kug and Ham 2012; Santoso et al. 2012; Terray et al. 2016; Xie et al. 2009, 2016; Kajtar et al. 2017). Several authors suggested that positive IOBs generate easterly wind anomalies over the western Pacific during boreal winter and spring as an atmospheric Kelvin wave response to the local diabatic warming (Annamalai et al. 2005; Terao and Kubota 2005; Kug and Kang 2006). Watanabe and Jin (2002) also argued that a positive IOB strengthens an anomalous low-level NorthWest Pacific Anticyclone centered on the Philippine Sea (NWPA, also referred to as Philippine Sea anticyclone or western North Pacific subtropical high in the literature; see Wang et al. 2000) during the mature-decayed phase of El Niño. Collectively, these atmospheric anomalies may fasten the transition from El Niño to La Niña since the associated zonal wind stress anomalies over the western Pacific force upwelling oceanic Kelvin waves that propagates eastward along the Equator and favor the transition to the La Niña phase (Kug and Kang 2006; Ohba and Ueda 2007; Ohba and Watanbe 2012; Kug and Ham 2012; Wang 2019). Some recent studies suggest, on the other hand, that the major forcing for the NWPA during boreal winter is from the central Pacific, as rainfall anomalies and associated diabatic warming over the IO are very modest during this season and, thus, cannot trigger an atmospheric Kelvin wave intruding into the western Pacific (Chen et al. 2016; Wu et al. 2017ab; Li and Hsu 2017; Li et al. 2017b). Luo et al. (2010) and Izumo et al. (2010) also found that IOD has highly significant impacts on both ENSO variability and predictability.

Our decoupling experiments allow to reinvestigate the significance of the IO feedback during boreal winter and spring in a consistent modeling framework, and may challenge the view that this IO negative feedback is weak during boreal winter (Li et al. 2017b). Moreover, what may be the impact of IO variability on the ENSO-ISM relationships despite the modest role of IOD on ISM suggested above?

To answer this question, Figure 8a-b displays the Niño-3.4 SST-ISMR lead-lag correlations and the monthly Niño-3.4 SST standard deviations in the FTIC and FSEIC

486 experiments in which IO or SEIO SST variability is removed (see Table 1 and Section 2c).
487 The negative Niño-3.4 SST-ISMR correlations before the ISM onset and ISMR standard
488 deviations during (early) boreal summer are substantially amplified in FTIC, while the ISMR
489 seasonal cycle remains the same (Fig. 8a, c-d). In other words, FTIC showed prominent
490 negative correlations with the Niño-3.4 SSTs *before rather than synchronous and after* the
491 ISM. These errors, already present in CTRL, are thus significantly amplified in FTIC. By
492 contrast, the simulated ISM and ENSO relationships in FSEIC closely resemble the observed
493 ones (Fig. 8a). FSEIC is able to recover the slow change of sign of the ISM-ENSO
494 correlations from positive to negative from year -1 to year 0 as observed. The differences
495 between the simulated and observed correlations for the different lags have been tested for
496 statistical significance with a Fisher Z transform approach (see Morrison 1990; pp 102-106)
497 and FSEIC is the only simulation, which does not show any statistical difference with
498 obseravtions at the 95% confidence level for any lags. Interestingly, this success is not related
499 to changes in the SST mean state (Figs. 1d and 2a) or ISMR seasonal cycle (Fig. 8d).
500 Evidences will be presented in this section to demonstrate that these large improvements are
501 related to changes in the characteristics of the model's El Niño during its decaying phase in
502 FSEIC.

503 Consistent with a strong damping of ENSO variability by IO variability, the Niño-3.4 SST
504 standard deviations increase significantly in FTIC (Fig. 8b). This increase is more prominent
505 during boreal spring and summer, which correspond to ENSO transitions. This suggests that
506 ENSO is less phase-locked to the annual cycle and that the length of ENSO events has
507 increased in FTIC. On the other hand, the Niño-3.4 SST variability is decreased in FSEIC
508 compared to both CTRL and FTIC. Interestingly, the Niño-3.4 SST monthly standard
509 deviations, as simulated by FSEIC, now match the observed Niño-3.4 SST standard
510 deviations during ENSO transitions (e.g. boreal spring). This suggests that ENSO events start
511 later or last shorter in FSEIC. In order to quantify more rigorously these differences between
512 the simulations, power spectra of the simulated Niño-3.4 SST time series are shown in Figure
513 9. Both FTIC and FSEIC spectra are strikingly different from CTRL spectrum, e.g. ENSO is
514 predominantly biennial or quasi-biennial in FSEIC while it lasts much longer in FTIC than in
515 CTRL and these results are statistically significant at the 95% confidence level (Fig. 9).
516 These important differences not only confirm that IO SSTs interact significantly with ENSO
517 in the SINTEX-F2 model, but also suggest that the spatial and temporal details of IO SST
518 variability play also a substantial role in the damping (or enhancement) and the length of the
519 simulated ENSO.

We first focus on the synchronous ISM-ENSO teleconnection during boreal summer. The rainfall and 850-hPa regressions onto the ISMR index in FTIC have spatial patterns similar to those in CTRL during JJ and AS (Fig. 6e-f). This demonstrates again that ENSO forcing is critical and that local ocean-atmosphere coupling is only a secondary factor for the generation of these anomalous patterns. However, consistent with a stronger (and partly erroneous) ENSO teleconnection during early summer (Fig. 8a,c), the rainfall and 850-hPa anomalies have greater amplitude almost everywhere in the Indo-Pacific region during JJ than AS in FTIC (Fig. 6e-f). The monsoon flux over the western IO is further increased during the whole ISM in FTIC compared to CTRL, resulting in enhanced rainfall over the Arabian Sea and western India (Fig. 6e-f). Interestingly, a negative IOD like rainfall pattern also emerges along the Equator in FTIC despite the absence of local coupling, demonstrating again the strong ENSO forcing on the regional rainfall pattern (Fig. 6e, f). In FSEIC, the 850-hPa wind and rainfall regressions onto the ISMR index show that the ISM-ENSO teleconnection gradually increases from JJ to AS in contrast to FTIC (Figs. 6g-h).

However, the interactions between the Indian and Pacific oceans need not to be restricted to the boreal summer, and may concern other seasons as well, and still be important for shaping the ENSO-ISM relationship. Indeed, the negative lagged correlations of ISM with the Niño-34 SSTs during boreal winter and spring preceding ISM are very different, while the lead correlations between ISM and the following Niño-34 SST anomalies are very similar among the simulations (Fig. 8a), suggesting that the IOB may play a prominent role in the ENSO damping and explain the relative success of FSEIC compared to both CTRL and FTIC.

In order to test the hypothesis that the IOB produces a direct forcing on ENSO itself in the simulations, Figs. 10 to 12 display lagged regressions of tropical Indo-Pacific SST, rainfall, 850-hPa wind and depth of 20°C isotherm anomalies during year +1 onto the December-January (DJ) Niño-3.4 SST index in the different simulations. Here, numerals such as 0 and +1 denote the ENSO developing (0) and decay (+1) years, respectively. Lagged regressions of 850-hPa stream function, 850- and 200-hPa velocity potential anomalies during February-March (FM) of year +1 onto DJ Niño-3.4 SST index are also displayed in Fig 13 in order to diagnose physical processes responsible of the differences in ENSO damping between the simulations.

First, the results confirm the robustness of the link between the decaying phase of El Niño events and the IOB in CTRL and FSEIC in which ocean-atmosphere coupling is (partly) active in the IO (Figs. 10a and 10c). As expected, the SST regression patterns over the tropical Pacific during FM(+1) show enhanced warming over the central and eastern Pacific

and a well-developed cold horseshoe signature in the extra-tropical Pacific in all experiments. However, the Pacific SST anomalies are more confined meridionally in the FSEIC experiment during FM(+1) and AM(+1) (Fig. 10c). The IO warming is basin-wide and uniform in CTRL and absent by design in FTIC (Fig. 10a-b). On the other hand, decoupling the SEIO enhances the warming in the other IO areas, especially over the western IO, and leads to a substantial anomalous SST equatorial gradient in the IO during FM(+1) (Fig. 10c). The modulation of the Walker circulation during El Niño induces local atmospheric subsidence (Fig. 13), which reduces cloud cover and forces near surface wind anomalies (Fig. 11) and surface heat fluxes over the IO, and, thus, initiates and sustains the basin-wide IOB warming in CTRL and FSEIC (Klein et al. 1999; Alexander et al. 2002; Schott et al. 2009).

Next, Fig. 10 illustrates that the Pacific SST anomalies during boreal spring and summer of the decaying phase of ENSO are different in the three simulations. First, the El Niño related warm anomalies persist up to the boreal summer of year +1 in FTIC, but have disappeared by the end of boreal spring in FSEIC, while CTRL exhibits an intermediate evolution of tropical Pacific SST anomalies between these two extreme scenarios. These results are consistent with the different seasonal phase locking of Niño-3.4 SST variability in the simulations (Fig. 8b). Cold equatorial Pacific SST anomalies emerge during boreal summer in FSEIC, signaling the beginning of a La Niña episode. Because of the slow response of the IO to ENSO forcing, the IOB persists until the following boreal summer in both CTRL and FSEIC (Figs. 10a, c). Surprisingly, IOB warming is more intense in FSEIC than in CTRL despite of the quick demise of the El Niño SST pattern in FSEIC.

In summary, these results first demonstrate that the IOB has a considerable impact on the anomalous climate during the decaying phase of ENSO in SINTEX-F2 (Figs. 10 to 12), consistent with previous studies (Kug and Kang 2006; Ohba and Ueda 2007; Ohba and Watanabe 2012; Terray et al. 2016; Cai et al. 2019; Wang 2019). However, the significant differences between FSEIC and CTRL highlight that the details of the IOB warming, especially the SST differences between the western IO and SEIO during late boreal winter, do also matter a lot, which is an important result of the present study.

In order to provide an explanation, we focus on the atmospheric circulation during FM(+1) (Fig. 13), when the differences in IO SST anomalies between the simulations are particularly well developed (Fig. 10 first row of panels). During the peak of El Niño, all the simulations show an enhanced convective activity over the central equatorial Pacific and reduced rainfall over the Maritime Continent (not shown) and such anomalous diabatic heating pattern is still seen during FM(+1), despite that Maritime Continent rainfall starts already to recover during

this season (Fig. 11 first row of panels). The associated 850- and 200-hPa velocity potential anomalies reveal that the Walker circulation shifts eastward in response to the diabatic warming (cooling) due to the enhanced (reduced) convection over the central Pacific (Maritime Continent). The 850-hPa stream function anomalies reveal a quadrupole structure straddling the Equator and asymmetric about it, which can be interpreted as a direct Rossby wave response to this anomalous convective pattern in all experiments (Fig. 13a,e,i). This four-cell structure plays a fundamental role in the maintenance of the rainfall and anomalous low-level circulation (Fig. 11, first row of panels), and is largely contributed by the tropical Pacific SST anomalies, which are very similar in the different simulations.

Focusing now on the IO and west Pacific, important differences in both the position and strength of the NWPA and its southern hemisphere counterpart exist between the simulations (Fig. 13a,e,i), which can directly be related to the different SST anomalies in the IO (Fig. 10 first row of panels). First, in both CTRL and FSEIC, in which IOB warming is present, these anticyclones are shifted eastward and the NWPA becomes stronger than its southern hemisphere counterpart. Second, these shifted anticyclones are further considerably strengthened in FSEIC compared to CTRL in response to a well-developed anomalous east-west circulation over the equatorial IO due to the enhanced SST zonal gradient in this run (Fig. 13j-k). Such an anomalous Walker cell over the IO is obviously absent in CTRL (Fig. 13b-c) in which the IOB warming is basin-wide and uniform (Fig. 10a). Moreover, this zonal dipole pattern in 850- and 200-hPa velocity potential anomalies in FSEIC, with anomalous ascending (descending) motion in the western (eastern) IO, is exactly similar to the observed pattern (see Fig. 5 of Li et al. 2017b for example).

Such modulation of the Walker circulation over the IO seems to be the key-factor to explain the strength of the IO negative feedback on ENSO during boral winter in FSEIC as positive rainfall anomalies are restricted to a small region in western IO and are seen in all the runs, including FTIC in which IOB is absent (Fig. 11 first row panel). It is therefore unlikely that such restricted rainfall anomaly is associated with a well-defined basin-wide diabatic heating anomaly, which may cause an atmospheric Kelvin wave response over the Western Pacific, consistent with the view of Chen et al. (2016) or Li et al. (2017b). On the other hand, the modulation of the Walker circulation over the IO induces more upper level convergence over the Maritime Continent and western Pacific in FSEIC (Fig. 13k), which strengthens considerably the NWPA and its southern counterpart (Fig. 13i), and the associated easterly wind anomalies over the western Pacific (Fig. 13l).

Thus, our results highlight that the IOB warming, but also the existence of an anomalous

622 SST gradient over the equatorial IO during boreal winter, are critical for the strength/position
623 of the NWPA, the generation of the associated anomalous easterlies over the western
624 equatorial Pacific and, finally, the turnabout of ENSO phases in our CGCM. As the equatorial
625 easterlies over the western equatorial Pacific are weaker in FTIC compared to CTRL and
626 much weaker than those in FSEIC (Fig. 13d,h,l), they may consequently have only a modest
627 influence on the Pacific SSTs one or two seasons later (Fig. 10b).

628   This working hypothesis, that the IOB warming and its spatial structure play a fundamental
629 role in hastening the ENSO transition through the generation of upwelling oceanic Kelvin
630 waves in both CTRL and FSEIC, is further supported by the regressions of the 20°C isotherm
631 depth (e.g. a proxy for the thermocline depth) anomalies during year +1 (Fig. 12). The slow
632 ocean dynamic adjustment in the tropical Pacific is different among the simulations. The
633 negative heat content anomalies (e.g. a shallower thermocline), which appear over the western
634 Pacific during the peak of El Niño, have a faster eastward propagation along the equatorial
635 Pacific in CTRL and FSEIC (Fig. 12a,c). This eastward propagation is very gradual in CTRL
636 (Fig. 12a), but somewhat abrupt, from AM to JJ of year +1, in FSEIC (Fig. 12c). Moreover,
637 FSEIC shows shallower 20°C isotherm anomalies than CTRL along the equatorial Pacific
638 (Fig. 12a,c). The enhanced zonal wind stress associated with the stronger easterly wind
639 anomalies over the western Pacific in FSEIC induces an enhanced vertical displacement of
640 the equatorial thermocline via Ekman pumping and the upwelling Kelvin wave response is
641 stronger in FSEIC. The arrival of these eastward Kelvin waves into the central equatorial
642 Pacific erodes the local surface warming (Fig. 10c). Consequently, lagging two to four
643 months behind the remote easterly wind anomalies over the western Pacific, cold SST
644 anomalies emerged quickly and expand westward over the central and eastern equatorial
645 Pacific during boreal summer of year +1 in FSEIC. Such ENSO transition is delayed in CTRL
646 (Fig. 10a) in agreement with the more modest NWPA and associated anomalous easterlies
647 over the western equatorial Pacific during FM(+1) seen in this run.

648   Consistent with the reversal of the equatorial anomalous SST gradient in the Pacific,
649 anomalous easterlies gradually emerge over the central Pacific during boreal summer of year
650 +1 in FSEIC (Fig. 11c). On the other hand, the easterly wind anomalies over the western
651 Pacific, seen during FM(+1) in FTIC, disappear quickly during AM(+1) (Fig. 11b). As a
652 consequence, both the El Niño-related thermocline and SST anomalies persist and we observe
653 a revival of the El Niño-related circulation and rainfall anomalous patterns during boreal
654 summer of year (+1) in FTIC. Finally, the evolution is again intermediate between these two
655 extremes in CTRL (Fig. 11a).

In agreement with these different El Niño evolutions in the simulations, we note that ISM is again highly deficient during boreal summer of the decaying phase of El Niño in FTIC, weak during JJ only in CTRL and, finally, normal or strong in FSEIC (Fig. 11 third and fourth rows). These assertions are further verified by computing regressions of boreal summer 200-hPa velocity potential anomalies onto the Niño-3.4 SST time series of the preceding boreal winter (Fig. 14). During El Niño decaying year, La Niña (El Niño) conditions prevail with a significantly strengthening (reduction) of the Walker circulation in the Indo-Pacific region in FSEIC (FTIC). Furthermore, strong (weak) upper level divergence is seen over the Indian region in FSEIC (FTIC) consistent with enhanced (reduced) diabatic heating associated with the ISM rainfall anomalies during boreal summer (Figs 11b-c third and fourth rows). Again, CTRL exhibits intermediate conditions between these two extremes with upper level convergence (e.g. subsidence) over India during JJ, but rather normal conditions in AS (Fig. 14a-b). These results demonstrate that the success to capture the seasonal evolution of the correlations between Niño-3.4 SSTs and ISMR in FSEIC (Fig. 8a) is plausibly related to the ability of this particular configuration to simulate correctly the space-time evolution of the tropical Pacific SSTs during the decaying phase of El Niño. In both CTRL and FSEIC, IOB is well developed during boreal summer of year +1 (Fig. 10a, c), but a weak (strong) ISM is simulated in CTRL (FSEIC) demonstrating that the remote ENSO forcing is still dominant in explaining the ISM response during the decaying year of El Niño. This may be understood by the fact that IOB SST anomalies are basin-wide, but of reduced amplitude during boreal summer of year +1, so that they are a significant factor for ISM variability if, and only if, tropical Pacific SST and circulation anomalies are rather weak at this stage (Figs. 10 and 11).

5. Summary and Discussion

5.a Summary

The present work examines the ability of current CGCMs in simulating the ISM-ENSO relationships. Consistent with previous studies (Terray et al. 2012; Jourdain et al. 2013; Sabeerali et al. 2019), we found that CGCMs used for climate projections or dynamical seasonal forecasting still exhibit significant errors with respect to this metric. Simulated ISM-ENSO correlations are already significant and negative several months before the ISM onset contrary to what is observed..The origins of these common errors in the simulation of the ISM-ENSO relationship are investigated based on several decoupling experiments performed

689   with the SINTEX-F2 CGCM.

690   First, a sensitivity experiment in which ENSO variability is removed (e.g. FTPC)
691   demonstrates that relationships between ISM and SST variability outside the tropical Pacific
692   are weak at interannual time scales in the absence of ENSO. As IODs still exist with
693   exaggerated amplitude in such decoupling experiment in which ENSO is removed (Fig. 2b,
694   see also Cretat et al. 2017, 2018), this suggests that IOD impact on ISM is not directly
695   responsible of the modulated ISM-ENSO relationship in this CGCM.

696   On the other hand, two others decoupling experiments in which IO SST variability is fully
697   removed (e.g. FTIC) or only in the SEIO (e.g. FSEIC) show a large spread in simulated
698   ENSO length and decay pace. ENSO becomes predominantly quasi-biennial in FSEIC while
699   ENSO lasts much longer in FTIC compared to CTRL. In FSEIC, cold SST and easterly wind
700   anomalies emerge quickly in the central equatorial Pacific during boreal summer of El Niño
701   decay years. By contrast, FTIC displays the persistence of a fully developed El Niño-like
702   pattern during the same time period. Finally, CTRL exhibits an intermediate evolution
703   between the above two extreme scenarios, despite that IOB warming is present in CTRL as in
704   FSEIC. As a consequence, weak ISMs are simulated during both El Niño developing and
705   decaying years in FTIC (and also in CTRL), while weak ISMs and El Niños tend to be
706   followed systematically by normal/strong ISMs and La Niñas in FSEIC. Further analysis
707   confirms that these differences in the decay phase of El Niño are responsible of the errors in
708   the simulated ISM-ENSO lead-lag relationships in CTRL.

709   Overall, our results suggest that progresses or changes in the simulation of the ISM-ENSO
710   relationships in CGCMs can be traced back to modifications of ENSO length and seasonal
711   phase-locking related to the impact of the IOB on ENSO and details of its spatial structure
712   (namely the equatorial SST gradient in the IO) during boreal winter. Surprisingly, the IOD or
713   the direct relationship between IO SSTs and ISM only play a secondary role in modulating
714   the ISM-ENSO relationship in our CGCM despite that it simulates an exaggerated IOD
715   variability, with or without ENSO, as many current CGCMs (Cai and Cowan 2013; Li et al.
716   2016; Annamalai et al. 2017).

717   Our results are also fully consistent with the suggestion that a fast ENSO transition in the
718   tropical Pacific and the persistence of IOB from boreal winter to boreal summer provide
719   favorable conditions for the occurrence of a strong ISM (Yang et al. 2007, 2010; Boschat et
720   al. 2011, 2012; Park et al. 2010; Chowdary et al. 2016, 2017). The emerging La Niña episode
721   will strengthen the ISM circulation and the IOB warming will tend to enhance the local

22

722 evaporation, moisten the atmosphere and reduce the moist stability; all factors tend to increase
723 ISM precipitation in FSEIC (Park et al. 2010).

724 5.b Discussion

725   In order to understand the physical processes, which are responsible of these different
726 evolutions, it is important to highlight first that mean-state errors are the same in the different
727 decoupled experiments analyzed here (Fig. 1a-d). This means that westward extension of cold
728 tongue bias and of the El Niño pattern in the tropical Pacific, which have been identified as
729 playing a seminal role in errors of the simulated ENSO decay pace and responsible of large
730 inter-model spread in CMIP3 or CMIP5 models (Kug and Ham 2012; Tao et al. 2016; Li et al.
731 2019) cannot explain directly (or alone) the differences among the runs.

732   The crucial role of the IOB warming in hastening the El Niño to La Niña transition (well
733 illustrated by the differences between the FTIC and CTRL) is consistent with previous studies
734 (Watanabe and Jin 2002; Kug and Kang 2006; Ohba and Ueda 2007; Xie et al. 2009, 2016;
735 Terray et al. 2016). On the other hand, the fact that the rapid decay of El Niño events and the
736 emergence of a La Niña developing event are likely to be the effect of the spatial details of the
737 IOB warming during boreal winter, rather than its simple existence or intensity per se, is an
738 important result of the present study as many recent works suggest that the IOB capacitor
739 effect is key mainly during the boreal summer of El Niño decay year, but not before (Chen et
740 al. 2016; Li et al. 20017b).

741   By comparing further CTRL and FSEIC, it is demonstrated that the simulation skill of the
742 ENSO decay pace and ISM-ENSO relationship is partly controlled by the (erroneous) SEIO
743 SST variability simulated in the CGCM. As illustrated by Fig. 2b, this SST variability bias is
744 characterized by an amplified seasonal cycle of SST variability with a double peak, one
745 during boreal winter (e.g. February) and the other during boreal fall (e.g. September).
746 Furthermore, Fig. 15b demonstrates that this erroneous double peak of SST variability in the
747 SEIO is a bias shared by most CMIP5 models, despite SINTEX-F2 and CMIP5 models differ
748 in their seasonal cycle of SST mean bias over SEIO (Figs. 2a and 15a). Most CMIP5 models
749 exhibit a cold bias throughout the seasonal cycle in the SEIO while the SINTEX-F2 model
750 exhibits a warm SST bias during boreal winter and a cold SST bias during boreal fall.

751   The cold SST mean bias and enhanced SST variability in the SEIO during boreal fall is a
752 well-known and long-standing problem of both the SINTEX-F2 and CMIP5 models (Fischer
753 et al. 2005; Terray et al. 2012; Prodhomme et al. 2014; Cretat et al. 2017; Cai and Cowan
754 2013; Li et al. 2015, 2016; Jourdain et al. 2016; Annamalai et al. 2017). Surprisingly, this

exaggerated SEIO SST variability during boreal fall, linked to the IOD, cannot explain the differences in ENSO evolution as described above.

On the other hand, the exaggerated SST variability in the SEIO during boreal winter in both SINTEX-F2 and CMIP5 models is less explored in the literature despite our analysis demonstrates its significant role on ENSO length and ISM-ENSO relationship. A working hypothesis for the existence of this SST bias is, however, the cold tongue bias and the associated excessive westward extension of El Niño SST warming along the equatorial Pacific found in most current CGCMs (Masson et al. 2012; Wang et al. 2014; Li and Xie 2012, 2014). These tropical Pacific biases have already been suggested to be very detrimental for a realistic simulation of both the ENSO-NWPA relationship and the negative IO feedback in CMIP5 models as they produce erroneous warm SST anomalies in the equatorial western Pacific during the El Niño decaying year, obstructing the formation of the anomalous NWPA (Kug and Ham 2012; Tao et al. 2016; Li et al. 2019). In order to investigate if the SEIO SST mean and variability biases are remotely forced by tropical Pacific errors in the SINTEX-F2 model, the annual cycle of monthly means and standard deviations of SEIO SSTs simulated in the FTPC and FTPC-obs decoupled experiments (see Section 2c) are displayed in Fig. 2. As ENSO variability is removed in both FTPC and FTPC-obs, but the Pacific mean-state errors are corrected only in FTPC-obs (Figs. 1e and 2a), the results suggest that SEIO biases during boreal fall have primarily local origins, as they are still present in both FTPC and FTPC-obs. On the other hand, those found during boreal winter are partly due to the remote Pacific forcing, as the erroneous SEIO SST variability during boreal winter is significantly damped in both FTPC and FTPC-obs, and the corresponding SST mean-state error is eliminated in FTPC-obs.

Thus, our results complement the previous studies, which focused primarily on the ocean-atmosphere and atmospheric processes over the equatorial western Pacific to explain the relationships between the ENSO decay pace, the NWPA and the local easterlies wind anomalies during boreal winter (Wang et al. 2000; Wu et al. 2017ab; Li et al. 2017b) and their degraded representation in current CGCMs (Kug and Ham 2012; Tao et al. 2016; Li et al. 2019). In SINTEX-F2, the negative IO feedback on ENSO is severely damped not only because of the local response (over the western equatorial Pacific) to the westward shift of the El Niño-related anomalies over the tropical Pacific, but also because such erroneous ENSO pattern produces an unrealistic remote forcing in the SEIO. The removal of the erroneous SEIO SST variability in FSEIC is sufficient to restore a realistic strength and position of the NWPA and associated equatorial easterlies and a correct ISM-ENSO relationship (Fig. 8)

related to the reduction of ENSO length. As most CMIP5 models exhibit exactly the same SST variability biases in the SEIO (Fig. 15a), it is not unlikely that correcting or removing the SEIO errors in these CGCMs will lead to similar improvements in their simulation of ENSO and ISM-ENSO relationships.

Past analysis of observations illustrate that the synchronous ISM-ENSO relationships has weakened, but that the impact of El Niño decaying phase on ISM has strengthened during recent decades (Fig 3; Yang et al. 2007, 2010; Boschat et al. 2012). This is fully consistent with the hypothesis of an enhanced negative IO feedback associated with the sustained IO warming (especially in the western IO), partly induced by anthropogenic forcing (Roxy et al. 2014) and the more frequent occurrence of the ENSO-related IO warming in recent decades (e.g., Boschat et al. 2012; Xie et al. 2016). Our numerical experiments do suggest that the IO is effectively an important climate element to explain the evolution of the ISM-ENSO system in the 20th century, as we are able to restore a realistic simulation of the lead-lag relationships between ISM and ENSO in a CGCM by simply eliminating the erroneous SST variability in the SEIO (Fig. 10a). In other words, it is conceivable that the intensified warming and negative feedback of the IO are important factors in the long-term variability of ENSO and ISM. This may have significant implications for our future projections of ENSO and ISM variations in a changing climate.

Additional testing with other CGCMs should therefore be performed in the future to promote a better understanding of the nature, seasonal timing and long-term behavior of the IO feedback on ENSO and ISM. However, the present work demonstrates that tropical SST biases in current CGCMs must be drastically reduced in order to shed new light on the mechanisms underlying the ISM variability. It is unlikely that state-of-the-art CGCMs will provide robust projections of ENSO or the ISM-ENSO relationship before prior reductions of systematic errors in the different tropical basins, like the cold tongue bias and the westward shift of the ENSO pattern in the tropical Pacific, the spurious IOD-like pattern in the IO or the unrealistic representation of the Atlantic zonal mode. Such systematic errors already preclude the robust attribution of the observed evolution of the ISM-ENSO relationships during the 20th century (illustrated in Fig. 3) to the anthropogenic forcing with the current CMIP5 simulations, as illustrated by the persistent controversies in the literature on this topic (Chen et al. 2010; Li and Ting 2015; Srivastava et al. 2015; Cash et al. 2017; Yun and Timmermann 2018; Feba et al. 2019; Bodai et al. 2020).

As illustrated in this work and summarized in two recent reviews (Cai et al. 2019; Wang 2019), interactions between the Indian, Pacific and also Atlantic basins play a seminal role in

823   explaining large-scale phenomena, like ENSO or ISM. From a modeling perspective, our

824   results further highlight that remote SST mean-state and variability errors in one basin, for

825   example the IO, can also interfere with SST biases in other basins like the Pacific and play a

826   key-role in the simulation of ENSO or ISM in current CGCMs (see also Terray et al. 2016).

827   In other words, this inter-basin framework is also fundamental to diagnose and correct the

828   severe biases still affecting current CGCMs.

829

830   **Appendix**

831

832   The SST nudging is performed inside the SST equation of the ocean model. We suppressed

833   the SST variability in a specific domain by applying a strong nudging of the SST toward a

834   SST climatology computed from a control experiment or observations (see Table 1 and

835   Section 2c for details). More precisely, this is done through a modification of the non-solar

836   heat flux provided by the atmosphere to the ocean by adding a correction term that is

837   proportional with the SST difference with the target climatology at each time step:

838

839    $$Q_{ns} = Q_{ns} + dq/dt*(SST - SST_{clim})$$

840

841   Q_{ns}: the nonsolar heat flux received from atmosphere

842   dq/dt: -2400 W m^{-2} K^{-1} (corresponds to the heat flux needed to warm a 50m thick ocean layer

843   of 1 K during 1 day)

844   SST_{clim}: the target SST daily climatology, after a linear interpolation at each time step of the

845   day

846

847   The very strong dq/dt constant used here implies that the SST variability is almost suppressed

848   in the selected domain. A Gaussian smoothing is finally applied in a transition zone in both

849   longitude and latitude at the limits of the SST restoring domains (see Table 1).

850

851   This approach is interesting because the ocean dynamics (e.g. also thermocline variations)

852   will be consistent with the SST in the ocean model, which is not the case when the SST is

853   changed in the coupling interface of the coupled model as it is commonly done in many

854   past/recent studies.

855

867   **References**

868   AchutaRao K, Sperber KR (2002) Simulation of the El Niño Southern Oscillation: Results
869   from the Coupled Model Intercomparison Project. Clim Dyn 19:191-209

870

871   AchutaRao K, Sperber KR (2006) ENSO simulation in coupled ocean-atmosphere models:
872   are the current models better? Clim Dyn 27:1-15 DOI 10.1007/s00382-006-0119-7
873

874   Achuthavarier D, Kirtman BP, Krishnamurty V, Huang B (2012) Role of the Indian Ocean in
875   the ENSO-Indian Summer Monsoon Teleconnection in the NCEP Climate Forecast System. J
876   Clim 25:2490-2508
877

878   Alexander MA, Bladé I, Newman M, Lanzante JR, Lau NC, Scott JD (2002) The atmospheric
879   bridge: the influence of ENSO teleconnections on air-sea interaction over the global oceans. J
880   Clim 15:2205-2231
881

882   Annamalai H, Xie SP, McCreary JP, Murtugudde R (2005) Impact of Indian Ocean Sea
883   surface temperature on developing El Niño. J Clim 18:302-319
884

885   Annamalai H, Hamilton K, Sperber KR (2007) The South Asian summer monsoon and its
886   relationship with ENSO in the IPCC AR4 simulations. J Clim 20:1071-1092
887   https://doi.org/10.1175/JCLI4035.1.
888

889   Annamalai H, Taguchi B, McCreary JP, Nagura M, Miyama T (2017) Systematic errors in
890   South Asian monsoon simulation: Importance of equatorial Indian Ocean processes. J Clim
891   30:8159-8178

892

893   Ashok K, Guan Z, Yamagata Y (2001) Impact of the Indian Ocean dipole on the relationship
894   between the Indian monsoon rainfall and ENSO. Geophys Res Lett 28:4499-4502

895

896   Ashok K, Guan Z, Saji NH, Yamagata T (2004), Individual and combined influences of
897   ENSO and the Indian Ocean dipole on the Indian summer monsoon. J Clim 17:3141-3155
898

899   Ashok K, Behera SK, Rao SA, Weng H, Yamagata T (2007) El Niño Modoki and its possible
900   teleconnection. J Geophys Res 112:C11007
901

902   Ashok K, Saji NH (2007) On the impacts of ENSO and Indian Ocean dipole events on sub-
903   regional Indian summer monsoon rainfall. Natural Hazards 42:273-285
904

905   Behera SK, Luo JJ, Masson S, Delecluse P, Gualdi S, Navarra A, Yamagata T (2005)
906   Paramount impact of the Indian Ocean dipole on the East African short rains: a CGCM study.
907   J Clim 18:4514-4530
908

909   Behera SK, Luo JJ, Masson S, Rao SA, Sakuma H, Yamagata T (2006) A CGCM study on
910   the interaction between IOD and ENSO. J Clim 19:1608-1705 doi: 10.1175/JCLI3797.1
911

912   Bellenger H, Guilyardi E, Leloup J, Lengaigne M, Vialard J (2014) ENSO representation in

climate models: from CMIP3 to CMIP5. Clim Dyn 42:1999-2018

Bodai T, Drotos G, Herein M, Lunkeit F, Lurarini V (2020) The Forced Response of the El Niño-Southern Oscillation-Indian Monsoon Teleconnection in Ensembles of Earth System Models. J Clim 33:6 2163-2182

Bollasina M, Ming Y (2013) The general circulation model precipitation bias over the southwestern equatorial Indian Ocean and its implications for simulating the South Asian monsoon. Clim Dyn 40:823-838

Boschat G, Terray P, Masson S (2011) Interannual relationships between Indian summer monsoon and Indo-Pacific coupled modes of variability during recent decades. Clim Dyn 37:1019-1043 doi: 10.1007/s00382-010-0887-y

Boschat G, Terray P, Masson S (2012) Robustness of SST teleconnections and precursory patterns associated with the Indian summer monsoon. Clim Dyn 38:2143-2165 doi: 10.1007/s00382-011-1100-7

Cai W, Cowan T (2013) Why is the amplitude of the Indian Ocean dipole overly large in CMIP3 and CMIP5 climate models? Geophys Res Lett 40 :1200-1205 doi: 10.1002/grl.50208

Cai W, Wu L, Lengaigne M, Li T, McGregor S, Kug J-S, Yu J-Y, Stuecker MF, Santoso A, Li X, Ham Y-G, Chikamoto Y, Ng B, McPhaden MJ, Du Y, Dommenget D, Jia F, Kajtar JB, Keenlyside, N., Lin, X., Luo, JJ, Martin-Rey M, Ruprich-Robert Y, Wang G, Xie SP, Yang Y, Kang SM, Choi J-Y, Gan B, Kim G-I, Kim C-E, Kim S, Kim J-H, Chang P (2019) Pantropical climate interactions. Science 363:6430 doi: 10.1126/science.aav4236

Cash BA, Barimalala R, Kinter JL, Altshuler EL, Fennessy MJ, Manganello JV et al (2017) Sampling variability and the changing ENSO-monsoon relationship. Clim Dyn 48:4071-4079. https://doi.org/10.1007/s00382-016-3320-3

Chen T-C (2003) Maintenance of summer monsoon circulations: a planetary-scale perspective. J Climate 16:2022-2037

Chen W, Dong B, Lu R (2010), Impact of the Atlantic Ocean on the multidecadal fluctuation of El Ni.o-Southern Oscillation-South Asian monsoon relationship in a coupled general circulation model. J Geophys Res 115:D17109 doi:10.1029/2009JD013596

Chen M-C, Li T, Shen X-Y et al. (2016) Relative roles of dynamic and thermodynamic processes in causing evolution asymmetry between El Niño and La Niña. J Clim 29:2201-2220 doi:10.1175/JCLI-D-15-0547.1

Cherchi A, Gualdi S, Behera S, Luo JJ, Masson S, Yamagata, T, Navarra A (2007) The influence of tropical Indian Ocean SST on the Indian summer monsoon. J Clim 20:3083-3105 doi:10.1175/JCLI4161.1

959

Cherchi A, Navarra A (2013) Influence of ENSO and of the Indian Ocean Dipole on the Indian summer monsoon variability. Clim Dyn 41:81-103 doi:10.1007/s00382-012-1602-y

Chowdary JS, Parekh A, Kakatkar R, Gnanaseelan C, Sriniva G, Singh P, Roxy M (2016) Tropical Indian Ocean response to the decay phase of El Nino in a coupled model and associated changes in south and east-Asian summer monsoon circulation and rainfall. Clim Dyn 47:831-844 doi:10.1007/s00382-015-2874-9

Chowdary JS, Harsha HS, Gnanaseelan C, Srinivas G, Parekh A, Pillai, P, Naidu CV (2017) Indian summer monsoon rainfall variability in response to differences in the decay phase of El Niño. Clim Dyn 48:2707-2727

Clarke AJ (2008) An Introduction to the Dynamics of El Niño and the Southern Oscillation. London: Academic Press pp 308

Cleveland WS, Devlin SJ (1988) Locally Weighted Regression: An Approach to Regression Analysis by Local Fitting. Journal of the American Statistical Association 83:596-610

Collins M and Coauthors (2010) The impact of global warming on the tropical Pacific Ocean and El Niño. Nat Geosci 3:391-397 doi:10.1038/ngeo868

Cretat J, Terray P, Masson S, Sooraj KP, Roxy MK (2017) Indian Ocean and Indian Summer Monsoon: relationships without ENSO in ocean-atmosphere coupled simulations. Clim Dyn 49:1429-1448 doi:10.1007/s00382-016-3387-x

Cretat J, Terray P, Masson S, Sooraj KP (2018) Intrinsic precursors and timescale of the tropical Indian Ocean Dipole: Insights from partially decoupled experiment. Clim Dyn 51:1311-1352 doi:10.1007/s00382-017-3956-7

Doi T, Behera SK, Yamagata T (2016) Improved seasonal prediction using the SINTEX-F2 coupled model. JAMES 8:1847-1867 doi:10.1002/2016MS000744

Dommenget D, V Semenov and M Latif (2006) Impacts of the tropical Indian and Atlantic Oceans on ENSO. Geophys Res Lett 33:L11701 doi:10.1029/2006GL025871

Drbohlav HKL, Gualdi S, Navarra A (2007) A diagnostic study of the Indian Ocean dipole mode in El Niño and non-El Niño years. J Clim 20:2961-2977 doi:10.1175/JCLI4153.1

Ebisuzaki W (1997) A method to estimate the statistical significance of a correlation when the data are serially correlated. J Clim 10:2147-2153

Feba F, Ashok K, Ravichandran M (2019) Role of changed Indo-Pacific atmospheric circulation in the recent disconnect between the Indian summer monsoon and ENSO. Clim Dyn 52:1461-1470

1005   Fischer A, Terray P, Guilyardi E, Delecluse P (2005) Two independent triggers for the Indian
1006   Ocean dipole/zonal mode in a coupled GCM. J Clim 18:3428-3449

1007

1008   Gadgil S, Vinayachandran PN, Francis PA, Gadgil S (2004) Extremes of the Indian summer
1009   monsoon rainfall, ENSO and equatorial Indian Ocean oscillation. Geophys Res Lett
1010   31:L12213 doi:10.1029/2004GL019733

1011

1012   Gadgil S, Rajeevan M, Nanjundiah R (2005) Monsoon prediction - why yet another failure?
1013   Curr Sci 84:1713-1719

1014

1015   Gadgil S, Rajeevan M, Francis PA (2007) Monsoon variability: links to major oscillations
1016   over the equatorial Pacific and Indian oceans. Curr Sci 93:182-194
1017
1018   Gershunov A, Schneider N, Barnett TP (2001) Low-frequency modulation of the ENSO-
1019   Indian monsoon rainfall relationship: Signal or noise? J Clim 14:2486-2492 https://doi.org/
1020   10.1175/1520-0442(2001)014,2486:LFMOTE.2.0.CO;2.
1021

1022   Gill AE (1980) Some simple solutions for heat-induced tropical circulation. Q J R Meteorol
1023   Soc 106:447-462
1024
1025   Gu DJ, Li T, Ji ZP et al (2010) On the phase relations between the western North pacific,
1026   Indian, and Australian monsoons. J Clim 23:5572-5589 doi:10.1175/2010 JCLI2761.1
1027

1028   Gualdi S, Guilyardi E, Navarra A, Masina S, Delecluse P (2003) The interannual variability
1029   in the tropical Indian Ocean as simulated by a CGCM. Clim Dyn 20:567-582
1030   doi:10.1007/s00382-002-0295-z
1031

1032   Ham YG, JS Kug (2014) ENSO phase-locking to the boreal winter in CMIP3 and CMIP5
1033   models. Clim Dyn 43:305-318

1034

1035   Huang B, Thorne Peter W et al (2017) Extended reconstructed sea surface temperature
1036   version 5 (ERSSTv5), upgrades, validations, and intercomparisons. J Clim 30:8179-8205
1037   https ://doi.org/10.1175/JCLI-D-16-0836.1

1038

1039   Huffman GJ, Adler RF, Morrissey MM, Bolvin DT, Curtis S, Joyce R, McGavock B,
1040   Susskind J (2001) Global precipitation at one-degree daily resolution from multisatellite
1041   observations. J Hydrometeor 2:36-50
1042

1043   Izumo T, Vialard J, Lengaigne M et al (2010) Influence of the state of the Indian Ocean
1044   Dipole on the following years El Niño. Nat Geosci 3:168-172
1045

1046   Jansen MF, D Dommenget and N Keenlyside (2009) Tropical Atmosphere-Ocean Interactions
1047   in a Conceptual Framework. J Clim 22(3):550-567.
1048

1049   Jourdain NC et al (2013) The Indo-Australian monsoon and its relationship to ENSO and IOD

1050 in reanalysis data and the CMIP3/CMIP5 simulations. Clim Dyn 41:3073-3102
1051

1052 Jourdain NC, Lengaigne M, Vialard J, Izumo T, Gupta AS (2016) Further insights on the
1053 influence of the Indian Ocean dipole on the following year's ENSO from observations and
1054 CMIP5 models. J Clim 29:637-658

1055

1056 Kajtar JB, Santoso A, England MH, Cai W (2017) Tropical climate variability: interactions
1057 across the Pacific, Indian, and Atlantic Oceans. Clim Dyn 48:2173-2190 doi:10.1007/s00382-
1058 016-3199-z
1059

1060 Keshavamurthy RN (1982) Response of the atmosphere to sea surface temperature anomalies
1061 over the equatorial Pacific and teleconnections of the Southern Oscillation. J Atmos Sci, 39,
1062 1241-1259
1063

1064 Kinter JL III, Miyakoda K, Yang S (2002) Recent changes in the connection from the Asian
1065 monsoon   to   ENSO.   J   Clim   15:1203-1215   doi:10.1175/1520-
1066 0442(2002)015<1203:RCITCF>2.0.CO;2

1067

1068 Kirtman B and Shukla J (2000) Influence of the Indian summer monsoon on ENSO. Q J R

1069 Meteor Soc 126:213-239 doi:10.1002/qj.49712656211

1070

1071 Klein SA, Soden BJ, Lau NC (1999) Remote sea surface temperature variations during
1072 ENSO: evidence for a tropical atmospheric bridge. J Clim 12:917-932, doi:10.1175/1520-
1073 0442(1999)012<0917:RSSTVD>2.0.CO;2.
1074

1075 Kosaka Y, Xie S-P, Lau NC, Vecchi GA (2013) Origin of seasonal predictability for summer
1076 climate over the Northwestern Pacific. PNAS 110:7574-7579

1077

1078 Krishna Kumar K, Rajagopalan B, Cane MA (1999) On the weakening relationship between
1079 the Indian monsoon and ENSO. Science 284:2156-2159
1080

1081 Krishna Kumar K, Rajagopolan B, Hoerling M, Bates G, Cane M (2006) Unraveling the
1082 mystery of Indian monsoon failure during El Nino. Science 314:115-119.

1083

1084 Krishna RPM, Rao SA, Srivastava A et al (2019) Impact of convective parameterization on
1085 the seasonal prediction skill of Indian summer monsoon. Clim Dyn 53:6227-6243
1086 https://doi.org/10.1007/s00382-019-04921-y

1087

1088 Krishnan R, Mujumdar M, Vaidya V, Ramesh KV, Satyan V (2003) The Abnormal Indian
1089 Summer Monsoon of 2000. J Clim 16:1177-1194

1090

1091 Krishnaswamy J, Vaidyanathan S, Rajagopalan B et al (2015) Non-stationary and non-linear
1092 influence of ENSO and Indian Ocean Dipole on the variability of Indian monsoon rainfall and
1093 extreme rain events. Clim Dyn 45:175-184 doi:10.1007/s00382-014-2288-0

Kucharski F, Bracco A, Yoo J, Molteni F (2007) Low- frequency variability of the Indian monsoon-ENSO relationship and the tropical Atlantic: The weakening of the 1980s and 1990s. J Clim 20:4255-4266

Kucharski F, Bracco A, Yoo J, Molteni F (2008) Atlantic forced component of the Indian monsoon interannual variability. Geophysical Research Letters 35:L04706

Kug J-S, Kang I-S (2006) Interactive feedback between ENSO and the Indian Ocean, J Clim 19:1784-1801

Kug J-S, Ham YG (2012) Indian Ocean feedback to the ENSO transition in a multi-model ensemble. J Clim 25:6942-6957 doi: 10.1175/JCLI-D-12-00078.1

Lau NC, Nath MJ (2000) Impact of ENSO on the variability of the Asian-Australian monsoons as simulated in GCM experiments. J Clim 13(24):4287-4309.

Lau NC, Nath MJ (2003) Atmosphere-ocean variations in the Indo-Pacific sector during ENSO episode. J Clim 16:3-20 doi: 10.1175/1520-0442(2003)016<0003:AOVITI>2.0.CO;2

Lau NC, Wang B (2006) Interactions between the Asian monsoon and the El Niño/Southern Oscillation. The Asian Monsoon, Wang B Ed, Springer/Praxis Publishing, New York, 478-512.

Lau NC, Nath MJ (2012) A Model Study of the Air-Sea Interaction Associated with the Climatological Aspects and Interannual Variability of the South Asian Summer Monsoon Development. J Clim 25:839-857 doi: 10.1175/JCLI-D-11-00035.1

Levine RC, Turner AG, Marathayil D, Martin GM (2013) The role of northern Arabian Sea surface temperature biases in CMIP5 model simulations and future projections of Indian summer monsoon rainfall. Clim Dyn 4:155-172

Li G, Xie S-P (2012) Origins of tropical-wide SST biases in CMIP multi-model ensembles. Geophys Res Lett 39:L22703. https ://doi.org/10.1029/2012G L0537 77

Li G, Xie S-P (2014) Tropical biases in CMIP5 multimodel ensemble: the excessive equatorial Pacific cold tongue and double ITCZ problems. J Clim 27:1765-1780

Li G, Xie S-P, Du Y (2015) Monsoon-induced biases of climate models in the tropical Indian Ocean. J Clim 28:3058-3072 doi:10.1175/JCLI-D-14-00740.1

Li G, Xie S-P, Du Y (2016) A Robust but Spurious Pattern of Climate Change in Model Projections over the Tropical Indian Ocean. J Clim 29 5589:5608

Li G, Xie S-P, He C et al (2017a) Western Pacific emergent constraint lowers projected increase in Indian summer monsoon rainfall. Nature Clim Change 7**:**708-712

https://doi.org/10.1038/nclimate3387

Li G, Jian Y, Yang S et al (2019) Effect of excessive equatorial Pacific cold tongue bias on the El Niño-Northwest Pacific summer monsoon relationship in CMIP5 multi-model ensemble. Clim Dyn 52:6195-6212

Li T, Wang B, Chang C-P et al (2003) A theory for the Indian Ocean dipole-zonal mode. J Atmos Sci 60:2119-2135 doi:10.1175/1520-0469(2003)060<2119:ATFTIO>2.0.CO;2

Li T, Hsu P-C (2017) Monsoon dynamics and its interactions with ocean. Fundamentals of Tropical Clim Dyn, Springer International Publishing, Cham, 236 pp, doi:10.1007/978-3-319-59597-9.

Li T, Wang B, Wu B et al. (2017b) Theories on formation of an anomalous anticyclone in western North Pacific during El Niño: A review. J. Meteor. Res., 31(6), 987-1006

Li X, Ting M (2015) Recent and future changes in the Asian monsoon-ENSO relationship:Natural or forced? Geophys Res Lett 42:3502-3512 https://doi.org/10.1002/2015GL063557

Li Z, Lin X, Cai W (2017c) Realism of modelled Indian summer monsoon correlation with the tropical Indo-Pacific affects projected monsoon changes. Sci Rep 7(1):1-7 doi: 10.1038/s41598-017-05225-z

Loschnigg J, Meehl GA, Webster PJ, Arblaster JM, Compo GP (2003) The Asian monsoon, the tropospheric biennial oscillation and the Indian Ocean dipole in the NCAR CSM. J Clim 16:2138-2158 doi:10.1175/1520-0442(2003)016<1617:TAMTTB>2.0.CO;2

Luo JJ, Masson S, Behera SK, Shingu S, Yamagata T (2005) Seasonal climate predictability in a coupled OAGCM using a different approach for ensemble forecasts. J Clim 18:4474-4497 doi:10.1175/JCLI3526.1

Luo JJ, Zhang R, Behera SK, Masumoto Y, Jin F-F, Lukas R, Yamagata T (2010) Interaction between El Niño and extreme Indian Ocean dipole, J Clim 23:726-742

Madec G (2008) NEMO ocean engine. Note du Pole de modelisation, Institut Pierre-Simon Laplace (IPSL) No 27. ISSN No 1288-1619

Masson S, Terray P, Madec G, Luo JJ, Yamagata T, Takahashi K (2012) Impact of intra-daily SST variability on ENSO characteristics in a coupled model. Clim Dyn 39:681-707

Meehl GA (1997) The south Asian monsoon and the tropospheric biennial oscillation (TBO). J Clim 10:1921-1943

Meehl GA, Arblaster JM (2002) The tropospheric biennial oscillation and the Asian-Australian monsoon rainfall. J Clim 15:722-744

Meehl GA, Arblaster JM, Loschnigg J (2003) Coupled ocean-atmosphere dynamical processes in the tropical Indian and Pacific oceans and the TBO. J Clim 16:2138-2158 doi:10.1175/2767.1

Mooley DA, Parthasarathy B (1983) Variability of the Indian summer monsoon and tropical circulation features. Mon Wea Rev 111:967-978

Morrison DF (1990) Multivariate statistical methods. McGraw-Hill, third edition, 495pp

Ohba M, Ueda H (2007) An Impact of SST Anomalies in the Indian Ocean in Acceleration of the El Nino to La Nina Transition. J Meteor Soc Jpn 85:335-348

Ohba M and M Watanbe (2012) Role of the Indo-Pacific Interbasin Coupling in Predicting Asymmetric ENSO Transition and Duration. J Clim, 25, 3321-3334.

Okumura YM, Ohba M, Deser C (2011) A proposed mechanism for asymmetric duration of El Nino and La Nina. J Clim 24:3822-3829

Pai DS, Sridhar L, Badwaik MR, Rajeevan M (2015) Analysis of the daily rainfall events over India using a new long period (1901-2010) high resolution (0.25×0.25) gridded rainfall data set. Clim Dyn 45:755-776

Park HS, Chiang JCH, Lintner BR and Zhang GJ (2010) The delayed effect of major El Niño events on Indian monsoon rainfall. J Clim 23:932-946

Parthasarathy B, Munot AA, Kothawale DR (1994) All-India monthly and seasonal rainfall series: 1871-1993. Theor Appl Climatol 49:217-224

Pillai PA, Annamalai H (2012) Moist dynamics of severe monsoons over South Asia: Role of the tropical SST. J Atmos Sci 69(1):97-115

Prodhomme C, Terray P, Masson S, Izumo T, Tozuka T, Yamagata T (2014) Impacts of Indian Ocean SST biases on the Indian Monsoon: as simulated in a global coupled model. Clim Dyn 42:271-290. doi:10.1007/s00382-013-1671-6

Prodhomme C, Terray P, Masson S, Boschat G, Izumo T (2015) Oceanic factors controlling the Indian Summer Monsoon Onset in a coupled model. Clim Dyn 44:977-1002. doi:10.1007/s00382-014-2200-y

Ramu DA, Chowdary JS, Ramakrishna SSVS, Kumar OSRUB (2018) Diversity in the representation of large-scale circulation associated with ENSO-Indian summer monsoon teleconnections in CMIP5 models. Theor Appl Climatol 132:465-478 https://doi.org/10.1007/s00704-017-2092-y

Rao KG, Goswami BN (1988) Interannual variations of sea surface temperature over the Arabian Sea and the Indian monsoon: a new perspective. Mon Weath Rev 116:558-568

Rao, SA, and Coauthors (2019) Monsoon Mission: A targeted activity to improve Monsoon prediction across scales. BAMS, Dec. 2019:2509-2532

Rasmusson EM, Carpenter TH (1983) The relationship between eastern equatorial Pacific sea surface temperature and rainfall over India and Sri Lanka. Mon Wea Rev 111:517-528 doi:10.1175/1520-0493(1983)111<0517:TRBEEP>2.0.CO;2

Rayner NA, Parker DE, Horton EB, Folland CK, Alexander LV, Rowell DP, Kent EC, Kaplan A (2003) Global analyses of sea surface temperature, sea ice, and night marine air temperature since the late nineteenth century. J Geophys Res 108(D14)4407   doi: 10.1029/2002JD002670

Reynolds RW, Smith TM, Liu C, Chelton DB, Casey KS, Schlax MG (2007) Daily high-resolution-blended analyses for sea surface temperature. J Clim 20:5473-5496. doi:10.1175/2007JCLI1824.1

Rodwell MJ, Hoskins BJ (2001) Subtropical Anticyclones and Summer Monsoons. J Clim 14:3192-3211

Roeckner E, Baüml G, Bonaventura L, Brokopf R, Esch M, Girogetta M, Hagemann S, Kirchner I, Kornblueh L, Manzini E, Rhodin A, Schlese U, Schulzweida U, Tompkins A (2003) The atmospheric general circulation model ECHAM 5, Part I. MPI Report, vol 349. Max-Planck-Institut für Meteorologie, Hamburg, pp 137

Roxy MK, Rikita K, Terray P, Masson S (2014) The curious case of Indian Ocean Warming. J Clim 27:8501-8508

Sabeerali CT, Ajayamohan RS, Rao SA (2019) Loss of predictive skill of indian summer monsoon rainfall in NCEP CFSv2 due to misrepresentation of Atlantic zonal mode. Clim Dyn 52:4599-4619 https://doi.org/10.1007/s00382-018-4390-1

Saha SK, Pokhrel S, Salunke K, Dhakate A, Chaudhari HS, Rahaman H, Sujith K, Hazra A, Sikka DR (2016) Potential predictability of Indian summer monsoon rainfall in NCEP CFSv2. JAMES 8:96-120 https://doi.org/10.1002/2015MS000542

Saha S et al (2014) The NCEP climate forecast system version 2. J Clim 27:2185-2208

Saji NH, Goswami BN, Vinayachandran PN, Yamagata T (1999) A dipole mode in the tropical Indian Ocean. Nature 401(6751):360-363. doi:10.1038/43855

Santoso A, England MH, Cai W (2012) Impact of Indo-Pacific Feedback Interactions on ENSO Dynamics Diagnosed Using Ensemble Climate Simulations, J Clim 25:7743-7763

Schott FA, Xie SP, McCreary JP (2009) Indian Ocean circulation and climate variability. Rev Geophys 47:RG1002 doi:10.1029/2007rg000245

1279
1280 Shukla J, Hagedorn R, Hoskins B, Kinter J, Marotzke J, Miller M, Palmer TN, Slingo J
1281 (2009) Strategies: Revolution in Climate Prediction is Both Necessary and Possible: A
1282 Declaration at the World Modelling Summit for Climate Prediction. Bull Amer Meteor Soc
1283 90:175-178.
1284
1285 Shukla RP, Huang B (2016) Interannual variability of the Indian summer monsoon associated
1286 with the air-sea feedback in the northern Indian Ocean. Clim Dyn 46:1977-1990
1287
1288 Sikka DR (1980) Some aspects of the large-scale fluctuations of summer monsoon rainfall
1289 over India in relations to fluctuations in the planetary and regional scale circulation
1290 parameters. J Earth Syst Sci 89:179-195 doi:10.1007/BF02913749
1291
1292 Spencer H, Sutton RT, Slingo JM, Roberts JM, Black E (2005) The Indian Ocean climate and
1293 dipole variability in the Hadley centre coupled GCMs. J Clim 18:2286-2307
1294
1295 Sperber KR, Annamalai, H, Kang I-S, Kitoh A, Moise A, Turner A, Wang B, Zhou T (2013)
1296 The Asian summer monsoon: an intercomparison of CMIP5 vs. CMIP3 simulations of the late
1297 20th century. Clim Dyn 41:2711-2744
1298
1299 Srivastava K, Srijith OP, Kshirsagar SR, Srivastava K (2015) Has modulation of Indian
1300 summer monsoon rainfall by sea surface temperature of the equatorial Pacific Ocean,
1301 weakened in recent years? Clim Dyn 45:2237-2254
1302
1303 Stuecker MF, Timmerman A, Jin FF, Chikamoto Y, Zhang W, Wittenberg AT, Widiasih E,
1304 Zhao S (2017) Revisiting ENSO/Indian Ocean dipole phase relationships. Geophys Res Lett
1305 44:2481-2492 doi: 10.1002/2016GL072308
1306
1307 Swapna and Coauthors (2015) The IITM earth system model. Bull Amer MeteorSoc
1308 96:1351–1367
1309
1310 Tao W, Huang G, Hu K et al (2016) A study of biases in simulation of the Indian Ocean basin
1311 mode and its capacitor effect in CMIP3/CMIP5 models. Clim Dyn 46**:**205-226
1312 https://doi.org/10.1007/s00382-015-2579-0
1313
1314 Taschetto AS, Gupta AS, Jourdain NC, Santoso A, Ummenhofer CC, England MH (2014)
1315 Cold tongue and warm pool ENSO events in CMIP5: mean state and future projections. J
1316 Clim 27:2861-2885
1317
1318 Taylor KE, Stouffer RJ, Meehl GA (2012) An overview of CMIP5 and the experiment design.
1319 BAMS 93:485-498.
1320
1321 Terao T, Kubota T (2005) East-west SST contrast over the tropical oceans and the post El
1322 Niño western North Pacific summer monsoon. Geophys Res Lett 32:L15706,
1323 doi:10.1029/2005GL023010.

Terray P (1995) Space/Time structure of monsoons interannual variability. *J Clim* 8:2595-2619

Terray P, Delecluse P, Labattu S, Terray L (2003) Sea Surface Temperature Associations with the Late Indian Summer Monsoon. Clim Dyn 21:593-618 DOI:10.1007/s00382-003-0354-0

Terray P, Guilyardi E, Fischer AS, Delecluse P (2005a) Dynamics of the Indian Monsoon and ENSO Relationships in the SINTEX global Coupled Model. *Clim Dyn* 24:145-168 DOI:10.1007/s00382-004-0479-9

Terray P, Dominiak S, Delecluse P (2005b) Role of the southern Indian Ocean in the transitions of the monsoon-ENSO system during recent decades. Clim Dyn 24:169-195 doi: 10.1007/s00382-004-0480-3

Terray P, Chauvin F, Douville H (2007) Impact of southeast Indian Ocean sea surface temperature anomalies on monsoon-ENSO dipole variability in a coupled ocean-atmosphere model. Clim Dyn 28:553-580 doi:10.1007/s00382-006-0192-y

Terray P, Kamala K, Masson S, Madec G, Sahai AK, Luo JJ, Yamagata T (2012) The role of the intra-daily SST variability in the Indian monsoon variability and monsoon-ENSO-IOD relationships in a global coupled model. Clim Dyn 39:729-754 doi:10.1007/s00382-011-1240-9

Terray P, Masson S, Prodhomme C, Roxy MK, Sooraj KP (2016) Impacts of Indian and Atlantic oceans on ENSO in a comprehensive modeling framework. Clim Dyn 46:2507-2533 doi: 10.1007/s00382-015-2715-x

Terray P, Sooraj KP, Masson S, Krishna RPM, Samson G, Prajeesh AG (2018) Towards a realistic simulation of boreal summer tropical rainfall climatology in state-of-the art coupled models: role of the background snow-free albedo. Clim Dyn, 50:3413-3439

Torrence C, Webster PJ (1999) Interdecadal changes in the ENSO-monsoon system. *J Clim* 12:2679-2690

Tourre y, White WB (1995) ENSO Signals in global upper-ocean temperature. J Phys Ocean 25:1317-1332

Turner AG, Annamalai H (2012) Climate change and the south Asian summer monsoon. Nat Clim Change 2:1-9

Ummenhofer CC, Sen Gupta A, Li Y, Taschetto AS, England MH (2011) Multi-decadal

modulation of the El Niño-Indian monsoon relationship by Indian Ocean variability. Env Res Lett 6:034,006

Valcke S (2006) OASIS3 user guide (prism_2-5). CERFACS technical report TR/CMGC/06/73, PRISM report no. 3, Toulouse, pp 64

Walker GT (1924) Correlation in seasonal variations of weather - A further study of world weather. Mon Wea Rev 53:252-254 doi:10.1175/1520-0493(1925)53<252:CISVOW>2.0.CO;2

Wang B (2006) The Asian Monsoon. Springer- Verlag/Praxis Publishing, New York, 787 pp.

Wang B, Wu RG, Fu XH (2000) Pacific-East Asian teleconnection: How does ENSO affect East Asian climate? J Clim 13:1517-1536 doi:10.1175/1520-0442(2000)013<1517:PEATHD>2.0.CO;2.

Wang B, Ding QH, Fu XH et al (2005) Fundamental challenge in simulation and prediction of summer monsoon rainfall. Geophys Res Lett 32:L15711 doi: 10.1029/2005GL02273412.

Wang B, Xiang BQ, Lee J-Y (2013) Subtropical high predictability establishes a promising way for monsoon and tropical storm predictions. PNAS USA, 110:2718-2722 doi:10.1073/pnas.1214626110

Wang C (2019) Three‑ ocean interactions and climate variability: a review and perspective. Clim Dyn 53:5119-5136

Wang C, Zhang L, Lee SK et al (2014) A global perspective on CMIP5 climate model biases. Nat Clim Chang 4:201-205

Wang H, Murtugudde R, Kumar A (2016) Evolution of Indian Ocean dipole and its forcing mechanisms in the absence of ENSO. Clim Dyn 47:2481-2500 doi:10.1007/s00382-016-2977-y

Wang H, Kumar A, Murtugudde R, Narapusetty B, Seip K (2019) Covariations between the Indian Ocean dipole and ENSO: A modeling study. Clim Dyn 53:5743-5761 doi: 10.1007/s00382-019-04895-x

Watanabe M, Jin F-F (2002) Role of Indian Ocean warming in the development of Philippine Sea anticyclone during ENSO. Geophys Res Lett 29:1478 doi: 10.1029/2001GL014318.

Webster PJ, Yang S (1992) Monsoon and ENSO: selectively interactive systems. Q J R Meteor Soc 118:877-926

Webster PJ, Hoyos CD (2010) Beyond the spring barrier? Nat Geosci 3:152-153 doi: 10.1038/ngeo800

Webster PJ, Magana V, Palmer TN, Shukla J, Tomas RA, Yanai M, Yasunari T (1998) Monsoons: processes, predictability and the prospects for prediction. J Geophys Res 103:14451-14510 doi:10.1029/97JC02719

Webster PJ, Moore AM, Loschnigg JP, Leben RR (1999) Coupled ocean-atmosphere dynamics in the Indian Ocean during 1997-1998. Nature 401:356-360 doi:10.1038/43848

Wieners CE, Dijkstra HA, de Ruijter WPM (2017a) The influence of the Indian Ocean on ENSO stability and flavor. J Clim 30:2601-2620 doi:10.1175/JCLI-D-16-0516.1

Wieners CE, Dijkstra HA, de Ruijter WPM (2017b) The influence of atmospheric convection on the interaction between the Indian Ocean and ENSO. J Clim 30:10155-10178 doi:10.1175/JCLI-D-17-0081.1

Wu B, Zhou TJ, Li T (2017a) Atmospheric dynamic and thermodynamic processes driving the western North Pacific anomalous anticyclone during El Niño. Part I: Maintenance mechanisms. J Clim 30:9621-9635 doi:10.1175/JCLID-16-0489.1

Wu B, Zhou TJ, Li T (2017b) Atmospheric dynamic and thermodynamic processes driving the western North Pacific anomalous anticyclone during El Niño. Part II: Formation processes. J Clim 30:9637-9650 doi:10.1175/JCLI-D-16-0495.1

Wu R, Kirtman BP (2004a) Impacts of the Indian Ocean on the Indian summer monsoon-ENSO relationship. J Clim 17:3037-3054

Wu R, Kirtman BP (2004b) Understanding the impacts of the Indian Ocean on ENSO variability in a coupled GCM. J Clim 17:4019-4031

Wu R, Kirtman BP (2005) Roles of Indian and Pacific Ocean air-sea coupling in tropical atmospheric variability. Clim Dyn 25:155-170

Wu R, Chen J, Chen W (2012) Different types of ENSO influences on the Indian summer monsoon variability. J Clim 25:903-920 https://doi.org/10.1175/JCLI-D-11-00039.1.

Xie SP, Hu K, Hafner J et al (2009) Indian Ocean capacitor effect on Indo-Western pacific climate during the summer following El Niño. J Clim 22:730-747 doi:10.1175/2008JCLI2544.1.

Xie SP, Kosaka Y, Du Y et al (2016) Indo-western Pacific Ocean capacitor and coherent climate anomalies in post-ENSO summer: a review. Adv Atmos Sci 33:411-432 doi:10.1007/s00376-015-5192-6

Yang JL, Liu QY, Xie S-P, et al (2007) Impact of the Indian Ocean SST basin mode on the Asian summer monsoon. Geophys Res Lett 34:L02708 doi:10.1029/2006GL028571

1457   Yang J, Liu Q, Liu Z (2010) Linking Observations of the Asian Monsoon to the Indian Ocean
1458   SST: Possible Roles of Indian Ocean Basin Mode and Dipole Mode. J Clim 23:5889-5902

1459

1460   Yang Y, Xie SP, Wu L, Kosoka Y, Lau NC, Vecchi GA (2015) Seasonality and predictability
1461   of the Indian Ocean Dipole mode: ENSO forcing and internal variability. J Clim 28:8021-
1462   8036

1463

1464   Yasunari T (1990) Impact of Indian monsoon on the coupled atmosphere/ocean system in the
1465   tropical Pacific. Meteor & Atmos Phys 44:29-41
1466
1467   Yun KS, Timmermann A (2018) Decadal monsoon-ENSO relationships reexamined.
1468   Geophys Res Lett 45:2014-2021 https://doi.org/10.1002/2017GL076912

1469

1470   Zhou Q, Duan W, Mu M, Feng R (2015) Influence of positive and negative Indian Ocean
1471   dipoles on ENSO via the Indonesian throughflow: results from sensitivity experiments. Adv
1472   Atmos Sci 32:783-793

1473

1474   Zhu J, Shukla J (2013) The Role of Air-Sea Coupling in Seasonal Prediction of Asia-Pacific
1475   Summer Monsoon Rainfall. J Clim 26:5689-5697 DOI:10.1175/JCLI-D-13-00190.1
1476

Figure captions

1478 **Figure 1**: **a)** SST means difference (°C) between CTRL (years 11-210) and HadISST1.1

1479 dataset (years 1979-2012); **b)** SST means difference (°C) between FTPC (years 11-110) and

1480 CTRL; **c)** SST means difference (°C) between FTIC (years 11-110) and CTRL; **d)** SST means

1481 difference (°C) between FSEIC (years 11-60) and CTRL and **e)** SST means difference (°C)

1482 between FTPC-obs (years 11-50) and CTRL. The nudging domains for FTPC, FTIC and

1483 FSEIC experiments are shown, respectively, in panels b (blue), c (green) and d (purple).

1484

1485 **Figure 2**: **a)** Monthly means of the SEIO (90°E-115°E and 0°S-10°S; unit: °C) SST time

1486 series from HadISST1.1 dataset (for the 1950-2012 and 1979-2012 periods) and the CTRL,

1487 FSEIC, FTPC and FTPC-obs experiments performed with the SINTEX-F2 model; **b)**

1488 Monthly standard deviations of the SEIO SST time series (unit: °C) from HadISST1.1 dataset

1489 (for the 1950-2012 and 1979-2012 periods) and the CTRL, FSEIC, FTPC and FTPC-obs

1490 experiments.

1491

1492 **Figure 3**: **a)** Lead-lag correlations between AIR time series and bi-monthly Niño-3.4 SSTs

1493 for different time periods, starting from the beginning of the previous year (e.g. year - 1) to

1494 the end of the following year of the monsoon (e.g. year +1) and **b)** Same as **a)** but using the

1495 ISMR time series derived from the IMD dataset. X-axis indicates the lag (in 2 months

1496 interval) for a 36 months period starting one year before the developing year of ISM and Y-

1497 axis is the amplitude of the correlation. Thus, the coefficients corresponding to -1, 0, +1

1498 month lags refer, respectively, to the correlations between AIR in year 0 (e.g. JJAS ISM

1499 rainfall) and April-May, June-July and August-September Niño-3.4 SSTs, also during year 0,

1500 and so on. Lead-lag correlations between ISMR time series estimated from GPCP dataset and

1501 bi-monthly Niño-3.4 SSTs for the period 1979-2012 are also displayed in panels **a** and **b** for

1502 comparison. All time series are detrended with a LOESS method (Cleveland and Devlin

1503 1988). Black diamond symbols indicate correlations that are above the 95% significance

1504 confidence level according to a phase-scrambling bootstrap test (Ebisuzaki 1997) with 999

1505 samples.

1506

1507 **Figure 4**: **a)** Lead-lag correlations between ISMR time series and bi-monthly Niño-3.4 SSTs,

1508 starting from the beginning of the previous year (e.g. year - 1) to the end of the following year

1509 of the monsoon (e.g. year +1) as simulated in the control experiments (CTRL) of the

1510   SINTEX-F2 and CFSv2 models and observed during the period 1979-2012. All time series

1511   are detrended with a LOESS method (Cleveland and Devlin 1988). Black diamond symbols

1512   indicate correlations that are above the 95% significance confidence level according to a

1513   phase-scrambling bootstrap test (Ebisuzaki 1997) with 999 samples. For observations, GPCP

1514   and HadISST1.1 datasets are used, respectively, for estimating the ISMR and Niño-3.4 SST

1515   time series; **b)** Monthly standard deviations of the Niño-3.4 SST time series from HadISST1.1

1516   dataset (for the 1950-2012 and 1979-2012 periods) and the CTRL experiments of the

1517   SINTEX-F2 and CFSv2 models; **c)** Monthly standard deviations of the ISMR time series

1518   from GPCP dataset (for 1979-2012 period) and the CTRL experiments of the SINTEX-F2 and

1519   CFSv2 models; **d)** Monthly means of the ISMR time series from GPCP dataset (for 1979-

1520   2012 period) and the CTRL experiments of the SINTEX-F2 and CFSv2 models.

1521

1522   **Figure 5**: Same as Fig. 4, but for historical runs of 25 CMIP5 models. For CMIP models, the

1523   period 1950-2000 is considered and time series are only linearly detrended. Statistical

1524   significance is not plotted, but correlation coefficients with an absolute value greater than

1525   0.25 are above the 95% significance confidence level according to a Student two-tailed t test.

1526   For observations, GPCP and HadISST1.1 datasets are used, respectively, for estimating the

1527   ISMR and Niño-3.4 SST time series. The ensembles mean and spread across the CMIP5

1528   models are also displayed. The spread is computed as the ensemble mean plus and minus the

1529   ensemble standard deviation (thick black circles in all panels).

1530

1531   **Figure 6**: **(a, b)** June-July and August-September mean rainfall (shading) and 850-hPa wind

1532   (vectors) anomalies regressed against the ISMR index (e.g. JJAS ISM rainfall) in the CTRL

1533   experiment; **(c, d)** same as **(a, b)** but for the FTPC experiment; **(e, f)** same as **(a, b)** but for the

1534   FTIC experiment and **(g, h)** same as **(a, b)** but for the FSEIC experiment. Unit for the rainfall

1535   and 850-hPa wind regression coefficients are, respectively, in mm/day by mm/day and m/s by

1536   mm/day. Only rainfall and 850-hPa wind regression coefficients above the 95% significance

1537   confidence level according to a phase-scrambling bootstrap test (Ebisuzaki 1997) with 999

1538   samples are shown.

1539

1540   **Figure 7**: **(a, b, c, d, e, f)** correlation coefficients between the ISMR index (e.g. JJAS ISM

1541   rainfall) and bi-monthly SST anomalies from February-March to December-January of year 0

1542   in the FTPC experiment. **(g, h, i, j, k, l)** same as **(a, b, c, d, e, f)** but for bi-monthly 200-hPa

1543   velocity potential anomalies. Correlation coefficients above the 95% significance confidence

1544   level according to a phase-scrambling bootstrap test (Ebisuzaki 1997) with 999 samples are

1545   contoured. In (**a, b, c, d, e, f**), correlation coefficients in the Pacific nudging domain are

1546   masked.

1547

1548   **Figure 8**: Same as Fig. 4, but for the FTIC and FSEIC experiments done with the SINTEX-

1549   F2 model. The results for the control (CTRL) and FTPC experiments performed with the

1550   SINTEX-F2 model are also displayed for comparison (only in panels **c** and **d** for FTPC).

1551

1552   **Figure 9**: Power spectra of Niño-34 SST anomalies for CTRL (red), FTIC (green) and FSEIC

1553   (blue) experiments. The bottom axis is the period (unit: year), the left axis is variance (unit:

1554   °C2) and both axes are in logarithm scale. Dashed red curves show the point-wise 95%

1555   confidence limits for the Niño-34 SST spectrum estimated from the CTRL experiment.

1556

1557   **Figure 10**: **a)** bi-monthly SST anomalies regressed against the December-January Niño-3.4

1558   SST time series for the following February-March, April-May, June-July, August-September

1559   and October-November (e.g. in year +1) in the CTRL experiment; **b)** same as **a)** but for the

1560   FTIC experiment; **c)** same as **a)** but for the FSEIC experiment. Unit for the SST regression

1561   coefficients is in K by K. Regression coefficients reaching the 10% significance level

1562   according to a phase-scrambling bootstrap test (Ebisuzaki 1997) with 999 samples are

1563   contoured.

1564

1565   **Figure 11: a)** bi-monthly mean rainfall (shading) and 850-hPa wind (vectors) anomalies

1566   regressed against the December-January Niño-3.4 SST time series for the following February-

1567   March, April-May, June-July, August-September and October-November (e.g. in year +1) in

1568   the CTRL experiment; **b)** same as **a)** but for the FTIC experiment; **c)** same as **a)** but for the

1569   FSEIC experiment. Unit for the rainfall and 850-hPa wind regression coefficients are,

1570   respectively, in mm/day by K and m/s by K. Only rainfall and 850-hPa wind regression

1571   coefficients reaching the 10% significance level according to a phase-scrambling bootstrap

1572   test (Ebisuzaki 1997) with 999 samples are shown.

1573

Figure 12: a) bi-monthly mean 20°C isotherm depth (a proxy for thermocline depth) anomalies regressed against the December-January Niño-3.4 SST time series for the following February-March, April-May, June-July, August-September and October-November (e.g. in year +1) in the CTRL experiment; **b)** same as **a)** but for the FTIC experiment; **c)** same as **a)** but for the FSEIC experiment. Unit for the 20°C isotherm depth regression coefficients is in m by K. Regression coefficients reaching the 10% significance level according to a phase-scrambling bootstrap test (Ebisuzaki 1997) with 999 samples are contoured.

Figure 13: **(a, b, c, d)** February-March 850-hPa stream function, 850-hPa velocity potential, 200-hPa velocity potential and 850-hPa zonal wind anomalies regressed against the preceding December-January Niño-3.4 SST time series in the CTRL experiment; **(e, f, g, h)** same as **(a, b, c, d)** but for the FTIC experiment; **(i, j, k, l)** same as **(a, b, c, d)** but for the FSEIC experiment. Units for the stream function and velocity potential regression coefficients are in 10^5 m^2 s^{-1} by K and for 850-hPa zonal wind in m s^{-1} by K. Regression coefficients reaching the 10% significance level according to a phase-scrambling bootstrap test (Ebisuzaki 1997) with 999 samples are contoured.

Figure 14: **(a, b)** June-July and August September 200-hPa velocity potential anomalies regressed against the preceding December-Januray Niño-3.4 SST time series in the CTRL experiment; **(c, d)** same as **(a, b)** but for the FTIC experiment; **(e, f)** same as **(a, b)** but for the FSEIC experiment. Units for the velocity potential regression coefficients are in 10^5 m^2 s^{-1} by K. Regression coefficients reaching the 10% significance level according to a phase-scrambling bootstrap test (Ebisuzaki 1997) with 999 samples are contoured.

Figure 15: **a)** Monthly means of the SEIO (90°E-115°E and 0°S-10°S; unit: °C) SST time series from HadISST1.1 dataset and the historical runs of 25 CMIP5 models; **b)** Monthly standard deviations of the SEIO SST time series from HadISST1.1 dataset and the historical runs of 25 CMIP5 models. All observed and simulated statistics are estimated from the period 1950-2000. The ensembles mean and spread across the CMIP5 models are also displayed. The spread is computed as the ensemble mean plus and minus the ensemble standard deviation (thick black circles in panels **a** and **b**).

Figure S1: **(a, b, c, d, e, f)** correlation coefficients between the ISMR index (e.g. JJAS ISM rainfall) and bi-monthly SST anomalies from February-March to December-January of year 0 in the CTRL experiment. **(g, h, i, j, k, l)** same as **(a, b, c, d, e, f)** but for bi-monthly 200 hPa velocity potential anomalies. Correlation coefficients above the 95% significance confidence level according to a phase-scrambling bootstrap test (Ebisuzaki 1997) with 999 samples are contoured.

Table captions

Table 1: Summary of the numerical experiments with their main characteristics, including length, nudging domain and SST climatology used for the nudging in the Indian or Pacific oceans decoupled experiments. The nudged experiments are the Forced Tropical Pacific Climatology (FTPC) run, the Forced Tropical Indian Climatology (FTIC) run, the Forced South-East Indian Climatology (FSEIC) run and, finally, the Forced Tropical Pacific observed Climatology (FTPC-obs) run. See text for more details. For the FTPC and FTPC-obs experiments only ocean grid-points in the Pacific are included in the correction or smoothing areas and, similarly, for the FTIC and FSEIC experiments for their respective domains. The different correction domains are also displayed in Figure 1b-d. The observed SST climatology used in the FTPC-obs experiment is derived from the AVHRR only daily Optimum Interpolation SST version 2 (OISSTv2) dataset for the 1982-2010 period (Reynolds et al. 2007).

Table S1: Description of the 25 Coupled Model Inter-comparison Project phase 5 (CMIP5) models used in our analysis. We use the historical coupled model experiments contributing to CMIP5 (see, url: http://pcmdi9.llnl.gov). Here, the first member of each model's ensemble of historical runs is used for all the analysis performed using CMIP5 models (e.g. Figures 5) and computations are done for the period 1950-2000. Each model dataset has been re-gridded into a 2.5°×2.5° horizontal grid, using a first-order remapping procedure implemented in the Climate Data Operators (https://code.zmaw.de/projects/cdo), before processing.
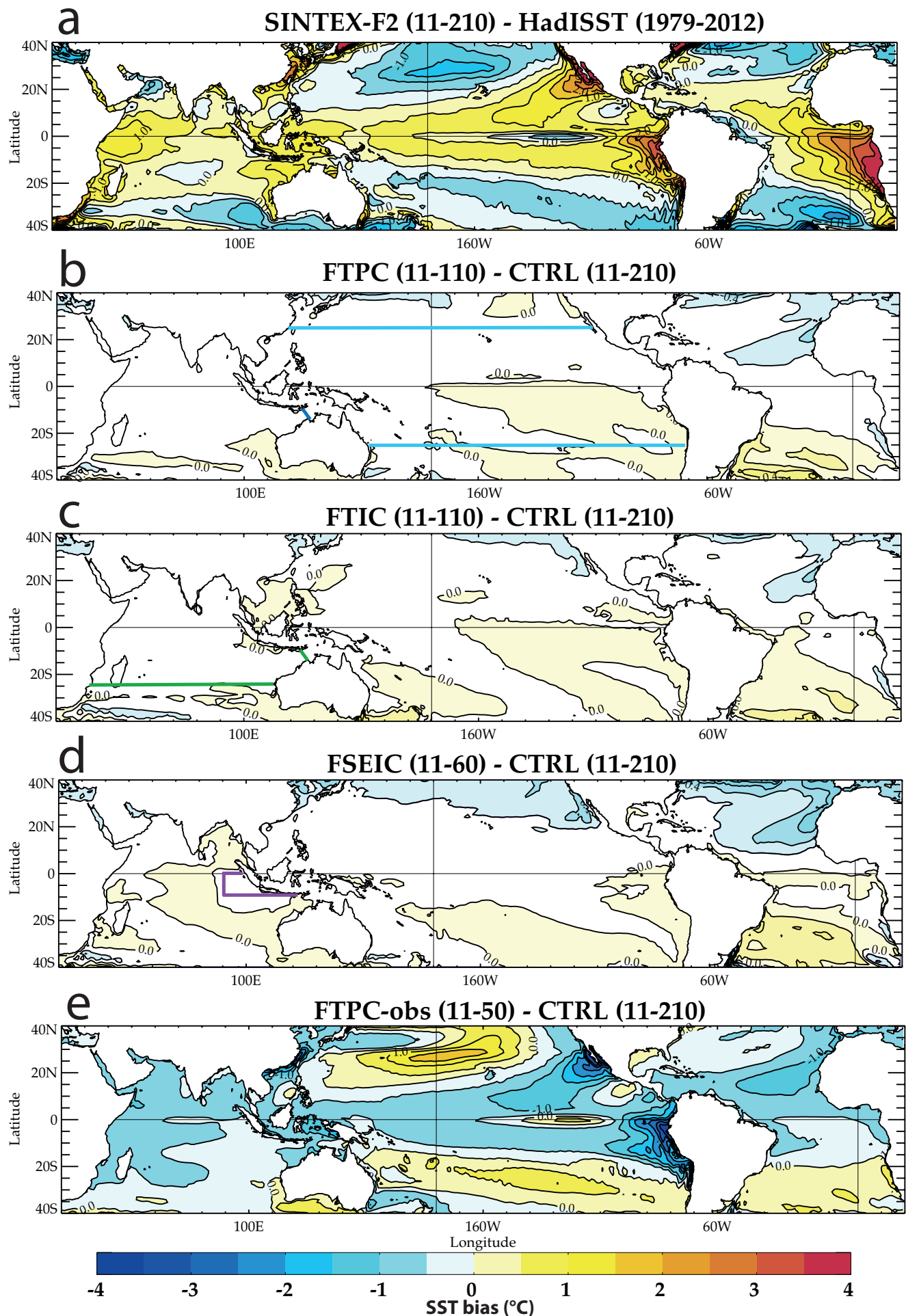
Figure 1: **a)** SST means difference (°C) between CTRL (years 11-210) and HadISST1.1 dataset (years 1979-2012); **b)** SST means difference (°C) between FTPC (years 11-110) and CTRL; **c)** SST means difference (°C) between FTIC (years 11-110) and CTRL; **d)** SST means difference (°C) between FSEIC (years 11-60) and CTRL and **e)** SST means difference (°C) between FTPC-obs (years 11-50) and CTRL. The nudging domains for FTPC, FTIC and FSEIC experiments are shown, respectively, in panels b (blue), c (green) and d (purple).
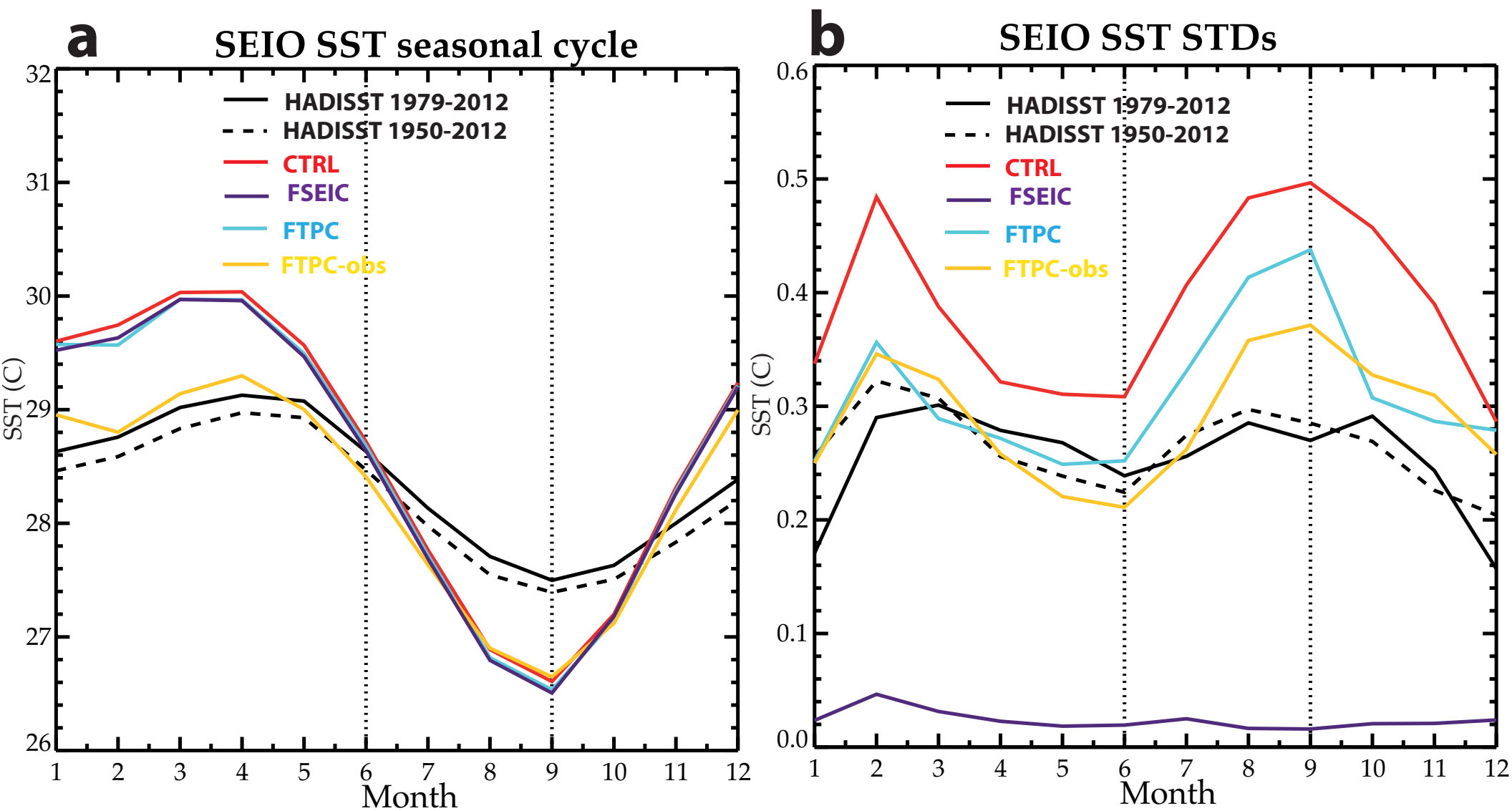
Figure 2: **a)** Monthly means of the SEIO (90°E-115°E and 0°S-10°S; unit: °C) SST time series from HadISST1.1 dataset (for the 1950-2012 and 1979-2012 periods) and the CTRL, FSEIC, FTPC and FTPC-obs experiments performed with the SINTEX-F2 model; **b)** Monthly standard deviations of the SEIO SST time series (unit: °C) from HadISST1.1 dataset (for the 1950-2012 and 1979-2012 periods) and the CTRL, FSEIC, FTPC and FTPC-obs experiments.
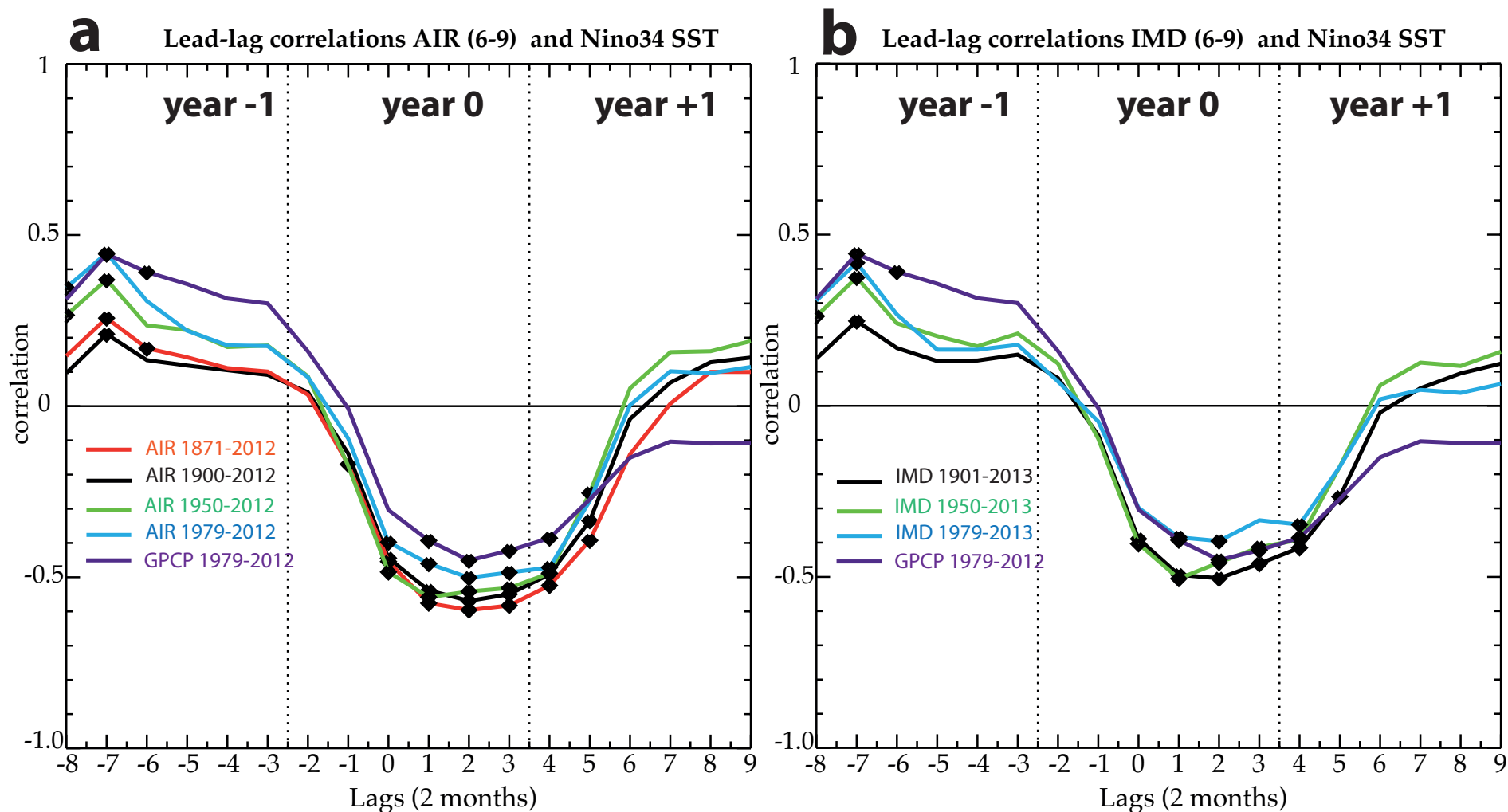
Figure 3: **a)** Lead-lag correlations between AIR time series and bi-monthly Niño-3.4 SSTs for different time periods, starting from the beginning of the previous year (e.g. year - 1) to the end of the following year of the monsoon (e.g. year +1) and **b)** Same as **a)** but using the ISMR time series derived from the IMD dataset. X-axis indicates the lag (in 2 months interval) for a 36 months period starting one year before the developing year of ISM and Y-axis is the amplitude of the correlation. Thus, the coefficients corresponding to -1, 0, +1 month lags refer, respectively, to the correlations between AIR in year 0 (e.g. JJAS ISM rainfall) and April-May, June-July and August-September Niño-3.4 SSTs, also during year 0, and so on. Lead-lag correlations between ISMR time series estimated from GPCP dataset and bi-monthly Niño-3.4 SSTs for the period 1979-2012 are also displayed in panels a and b for comparison. All time series are detrended with a LOESS method (Cleveland and Devlin 1988). Black diamond symbols indicate correlations that are above the 95% significance confidence level according to a phase-scrambling bootstrap test (Ebisuzaki 1997) with 999 samples.
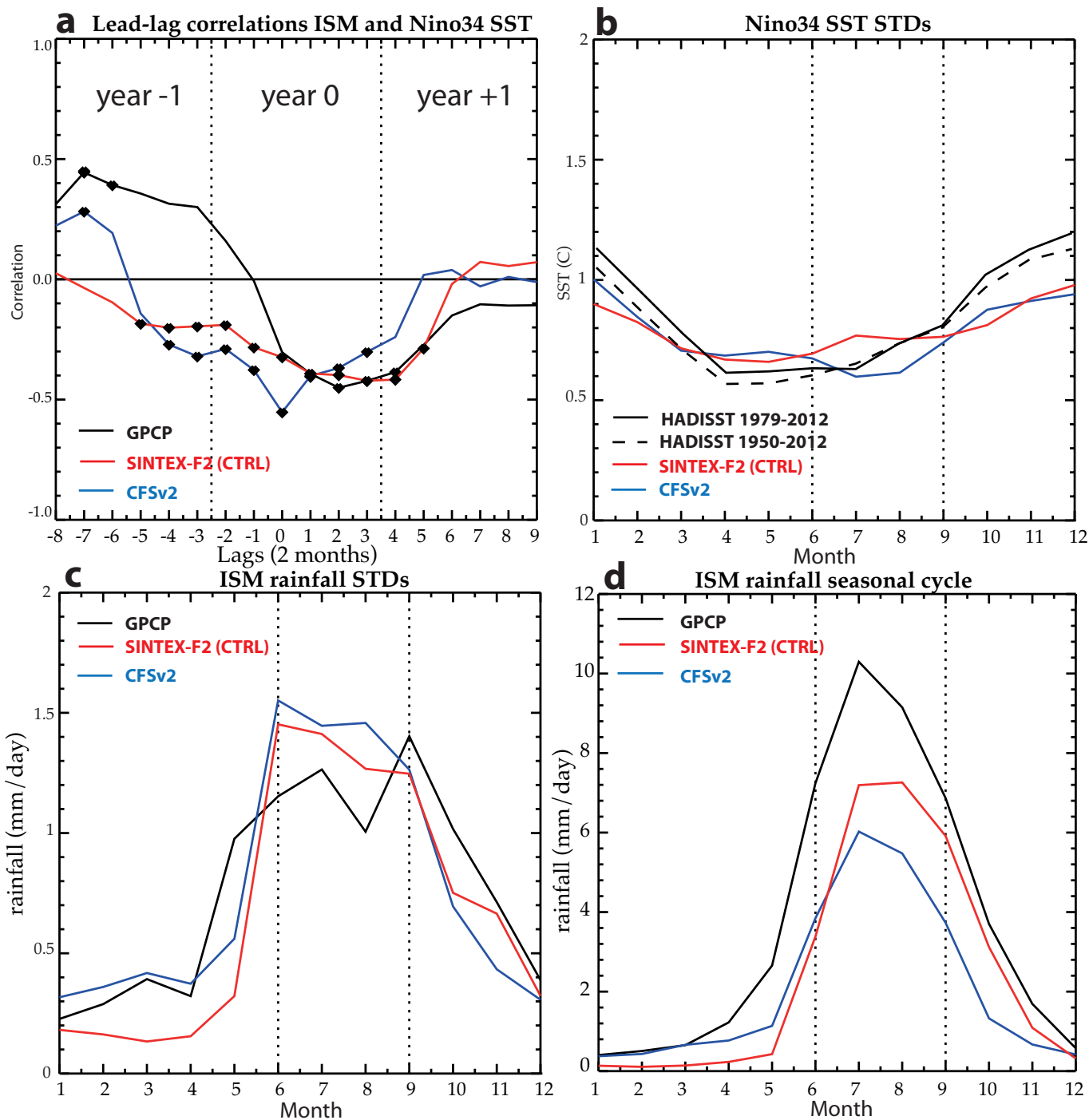
Figure 4: **a)** Lead-lag correlations between ISMR time series and bi-monthly Niño-3.4 SSTs, starting from the beginning of the previous year (e.g. year - 1) to the end of the following year of the monsoon (e.g. year +1) as simulated in the control experiments (CTRL) of the SINTEX-F2 and CFSv2 models and observed during the period 1979-2012. All time series are detrended with a LOESS method. Black diamond symbols indicate correlations that are above the 95% significance confidence level according to a phase-scrambling bootstrap test (Ebisuzaki 1997) with 999 samples. For observations, GPCP and HadISST1.1 datasets are used, respectively, for estimating the ISMR and Niño-3.4 SST time series; **b)** Monthly standard deviations of the Niño-3.4 SST time series from HadISST1.1 dataset (for the 1950-2012 and 1979-2012 periods) and the CTRL experiments of the SINTEX-F2 and CFSv2 models; **c)** Monthly standard deviations of the ISMR time series from GPCP dataset (for 1979-2012 period) and the CTRL experiments of the SINTEX-F2 and CFSv2 models; **d)** Monthly means of the ISMR time series from GPCP dataset (for 1979-2012 period) and the CTRL experiments of the SINTEX-F2 and CFSv2 models.
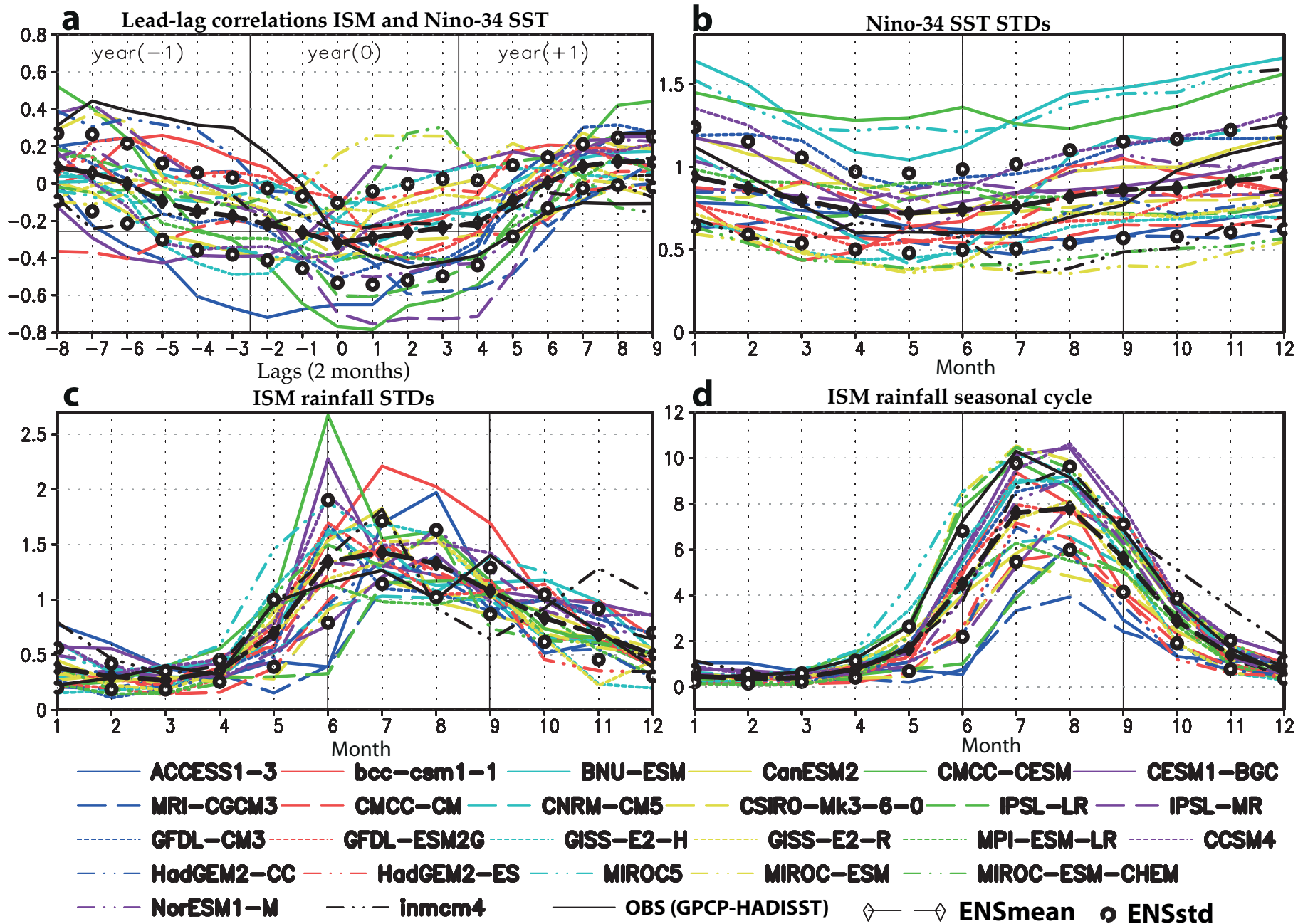
Figure 5: Same as Fig. 4, but for historical runs of 25 CMIP5 models. For CMIP models, the period 1950-2000 is considered and time series are only linearly detrended. Statistical significance is not plotted, but correlation coefficients with an absolute value greater than 0.25 are above the 95% significance confidence level according to a Student two-tailed t test. For observations, GPCP and HadISST1.1 datasets are used, respectively, for estimating the ISMR and Niño-3.4 SST time series. The ensembles mean and spread across the CMIP5 models are also displayed. The spread is computed as the ensemble mean plus and minus the ensemble standard deviation (thick black circles in all panels).

Figure 6: **(a, b)** June-July and August-September mean rainfall (shading) and 850-hPa wind (vectors) anomalies regressed against the ISMR index (e.g. JJAS ISM rainfall) in the CTRL experiment; **(c, d)** same as **(a, b)** but for the FTPC experiment; **(e, f)** same as **(a, b)** but for the FTIC experiment and **(g, h)** same as **(a, b)** but for the FSEIC experiment. Unit for the rainfall and 850-hPa wind regression coefficients are, respectively, in mm/day by mm/day and m/s by mm/day. Only rainfall and 850-hPa wind regression coefficients above the 95% significance confidence level according to a phase-scrambling bootstrap test (Ebisuzaki 1997) with 999 samples are shown.
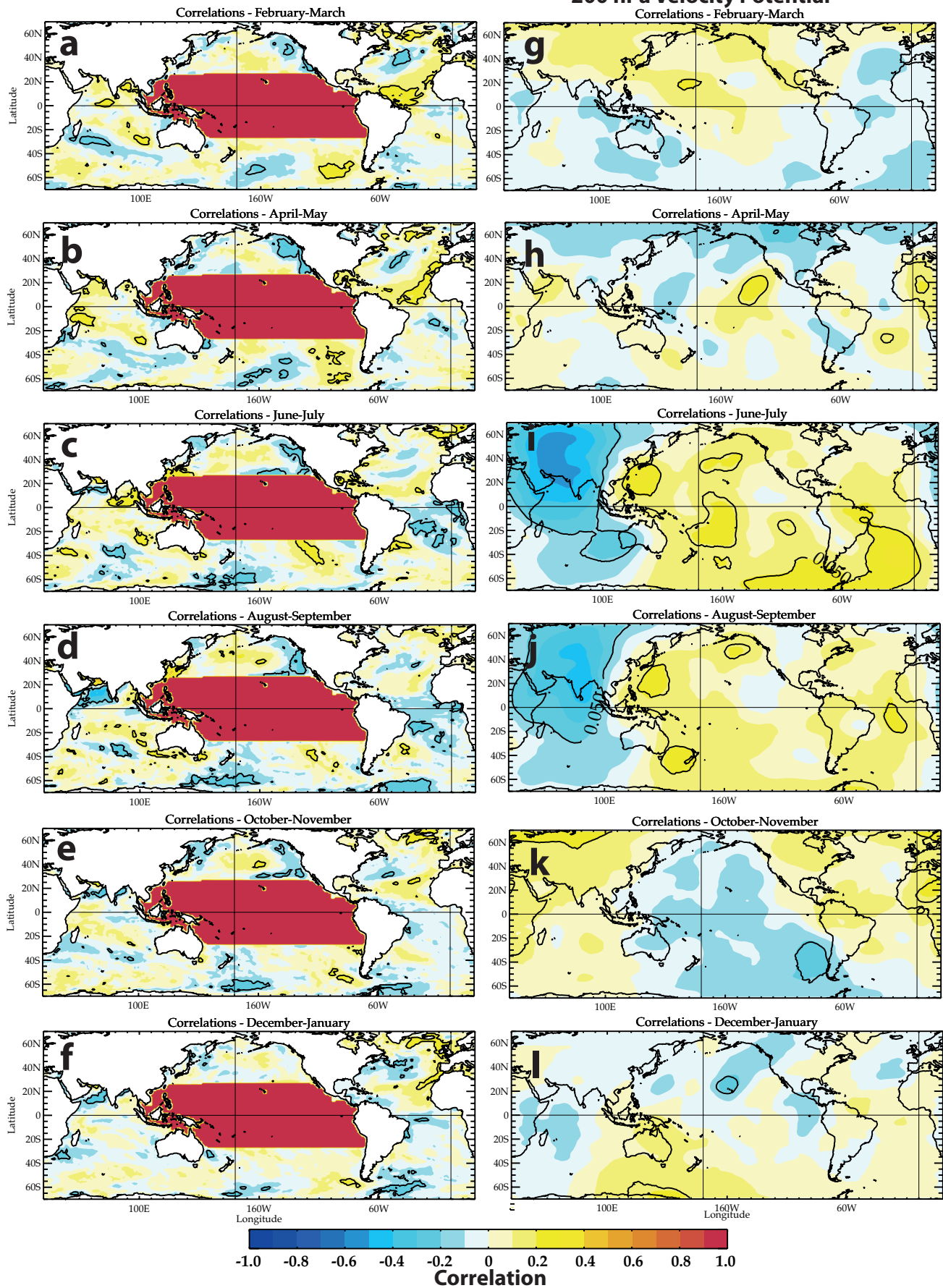
Figure 7: **(a, b, c, d, e, f)** correlation coefficients between the ISMR index (e.g. JJAS ISM rainfall) and bi-monthly SST anomalies from February-March to December-January of year 0 in the FTPC experiment. **(g, h, i, j, k, l)** same as **(a, b, c, d, e, f)** but for bi-monthly 200-hPa velocity potential anomalies. Correlation coefficients above the 95% significance confidence level according to a phase-scrambling bootstrap test (Ebisuzaki 1997) with 999 samples are contoured. In **(a, b, c, d, e, f)**, correlation coefficients in the Pacific nudging domain are masked.
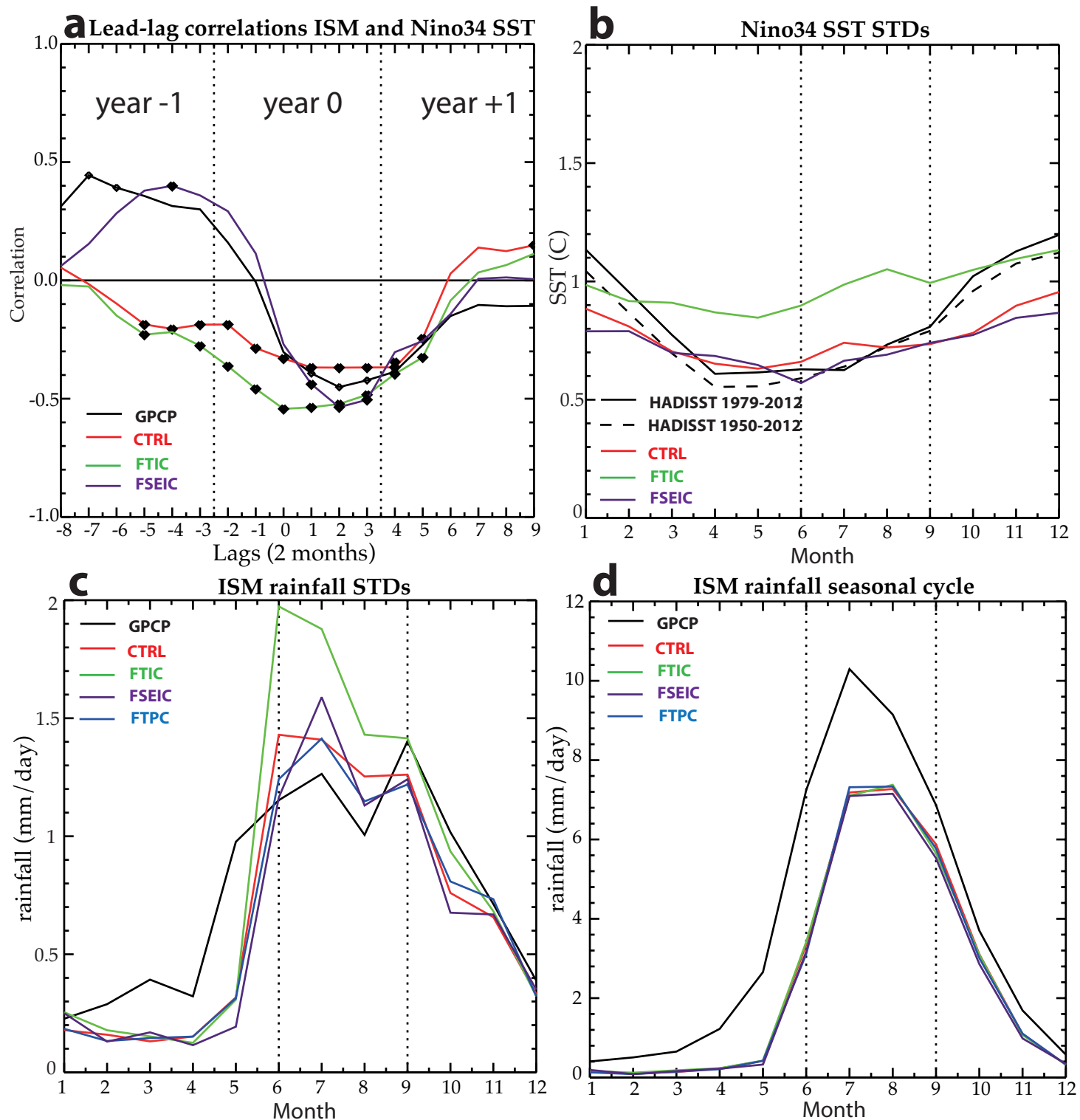
Figure 8: Same as Fig. 4, but for the FTIC and FSEIC experiments done with the SINTEX-F2 model. The results for the control (CTRL) and FTPC experiments performed with the SINTEX-F2 model are also displayed for comparison (only in panels **c** and **d** for FTPC).
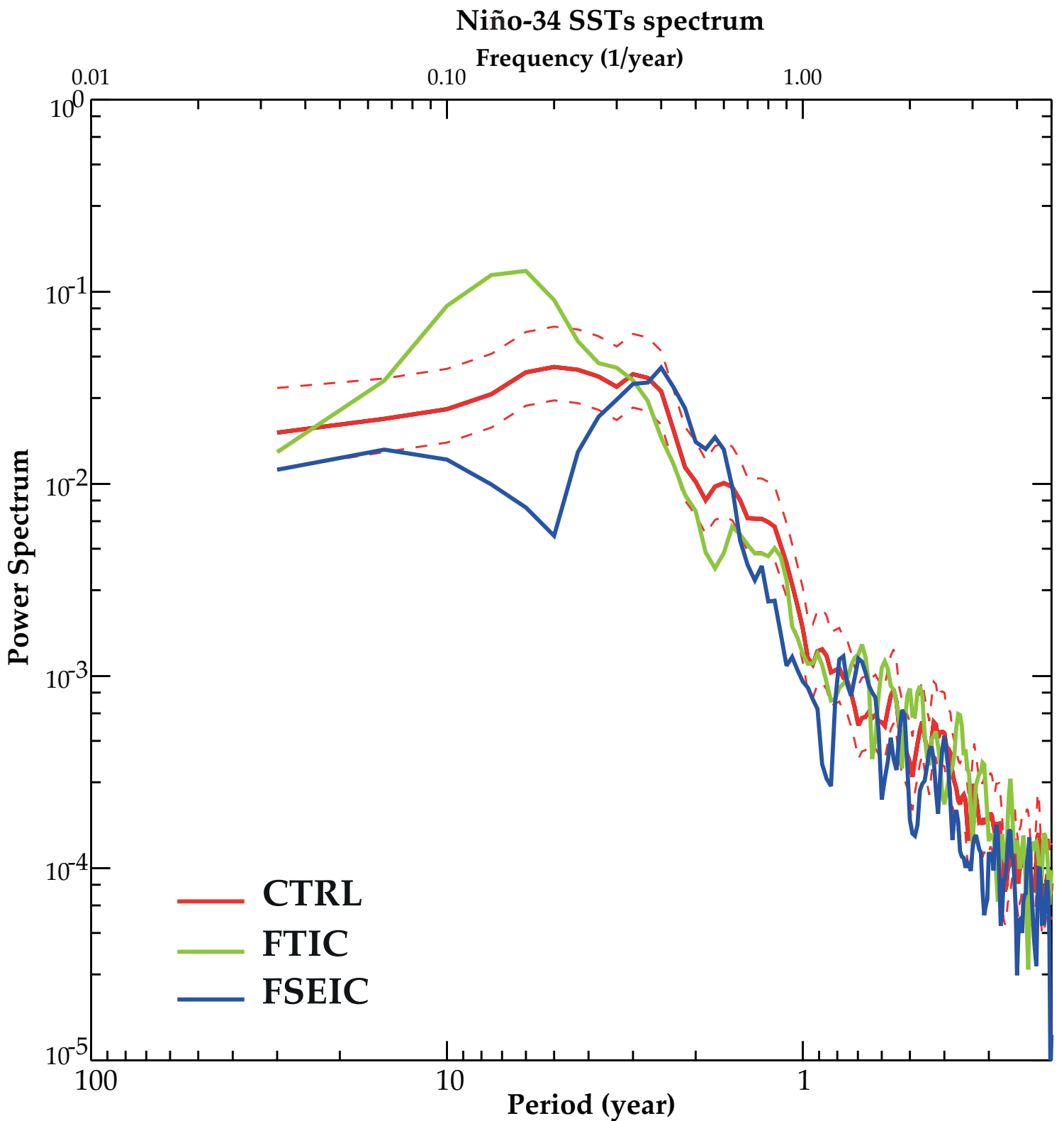
Figure 9: Power spectra of Niño-34 SST anomalies for CTRL (red), FTIC (green) and FSEIC (blue) experiments. The bottom axis is the period (unit: year), the left axis is variance (unit: °C2) and both axes are in logarithm scale. Dashed red curves show the point-wise 95% confidence limits for the Niño-34 SST spectrum estimated from the CTRL experiment.

Figure 10: **a)** bi-monthly SST anomalies regressed against the December-January Niño-3.4 SST time series for the following February-March, April-May, June-July, August-September and October-November in the CTRL experiment; **b)** same as **a)** but for the FTIC experiment ; **c)** same as **a)** but for the FSEIC experiment. Unit for the SST regression coefficients is in K by K. Regression coefficients reaching the 10% significance level according to a phase-scrambling bootstrap test (Ebisuzaki 1997) with 999 samples are contoured.

Figure 11: **a)** bi-monthly mean rainfall (shading) and 850-hPa wind (vectors) anomalies regressed against the December-January Niño-3.4 SST time series for the following February-March, April-May, June-July, August-September and October-November in the CTRL experiment; **b)** same as **a)** but for the FTIC experiment; **c)** same as **a)** but for the FSEIC experiment. Unit for the rainfall and 850-hPa wind regression coefficients are, respectively, in mm/day by K and m/s by K. Only rainfall and 850-hPa wind regression coefficients reaching the 10% significance level according to a phase-scrambling bootstrap test (Ebisuzaki 1997) with 999 samples are shown.
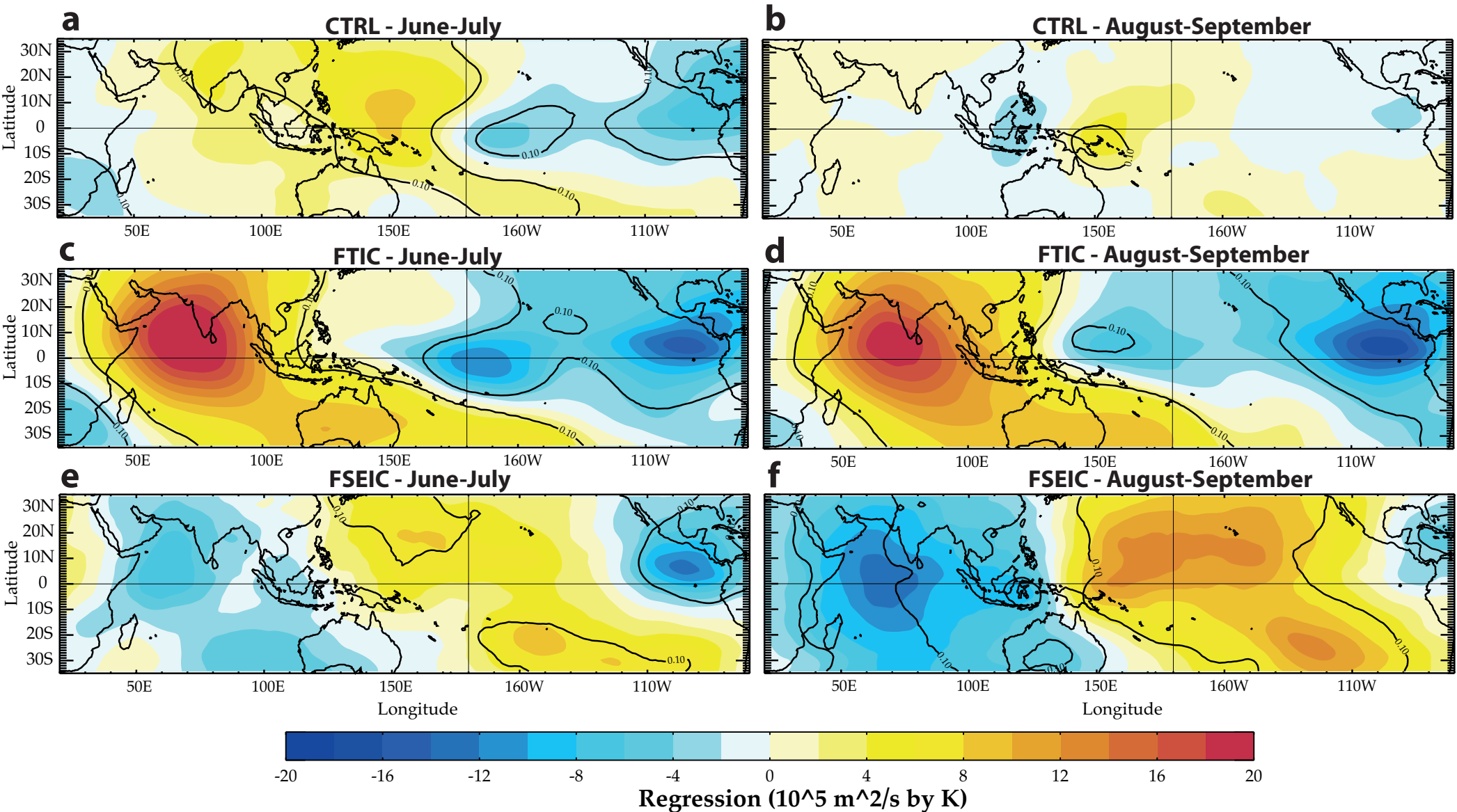
Figure 12: **a)** bi-monthly mean 20°C isotherm depth (a proxy for thermocline depth) anomalies regressed against the December-January Niño-3.4 SST time series for the following February-March, April-May, June-July, August-September and October-November in the CTRL experiment; **b)** same as **a)** but for the FTIC experiment ; **c)** same as **a)** but for the FSEIC experiment. Unit for the 20°C isotherm depth regression coefficients is in m by K. Regression coefficients reaching the 10% significance level according to a phase-scrambling bootstrap test (Ebisuzaki 1997) with 999 samples are contoured.
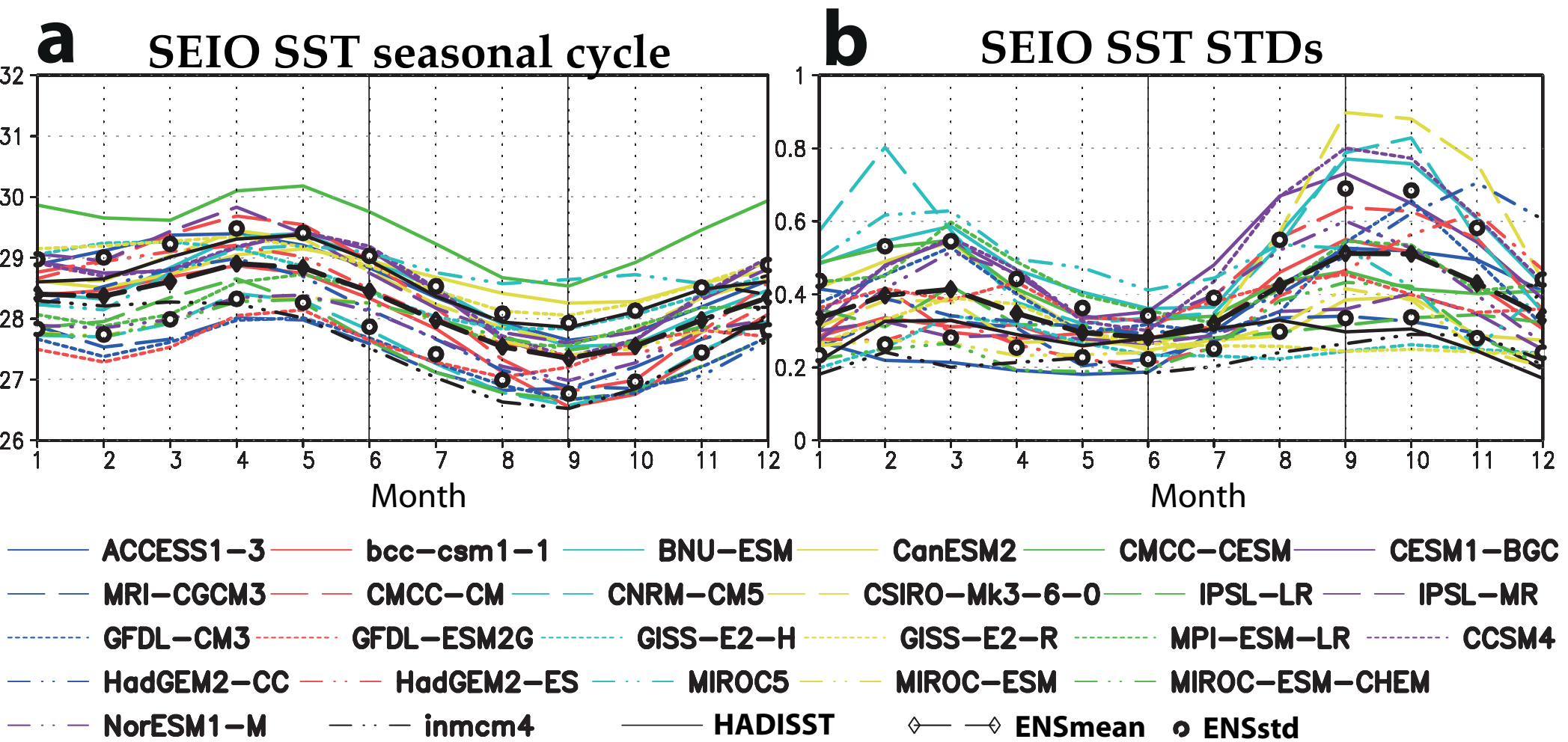
Figure 13: **(a, b, c, d)** February-March 850-hPa stream function, 850-hPa velocity potential, 200-hPa velocity potential and 850-hPa zonal wind anomalies regressed against the preceding December-January Niño-3.4 SST time series in the CTRL experiment; **(e, f, g, h)** same as **(a, b, c, d)** but for the FTIC experiment; **(i, j, k, l)** same as **(a, b, c, d)** but for the FSEIC experiment. Units for the stream function and velocity potential regression coefficients are in 105 m2 s-1 by K and for 850-hPa zonal wind in m s-1 by K. Regression coefficients reaching the 10% significance level according to a phase-scrambling bootstrap test (Ebisuzaki 1997) with 999 samples are contoured.

Figure 14: **(a, b)** June-July and August September 200-hPa velocity potential anomalies regressed against the preceding December-Januray Niño-3.4 SST time series in the CTRL experiment; **(c, d)** same as **(a, b)** but for the FTIC experiment; **(e, f)** same as **(a, b)** but for the FSEIC experiment. Units for the velocity potential regression coefficients are in 105 m2 s-1 by K. Regression coefficients reaching the 10% significance level according to a phase-scrambling bootstrap test (Ebisuzaki 1997) with 999 samples are contoured.
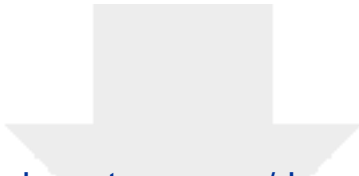
Figure 14: **a)** Monthly means of the SEIO (90°E-115°E and 0°S-10°S; unit: °C) SST time series from HadISST1.1 dataset and the historical runs of 25 CMIP5 models; **b)** Monthly standard deviations of the SEIO SST time series from HadISST1.1 dataset and the historical runs of 25 CMIP5 models. All observed and simulated statistics are estimated from the period 1950-2000. The ensembles mean and spread across the CMIP5 models are also displayed. The spread is computed as the ensemble mean plus and minus the ensemble standard deviation (thick black circles in panels **a** and **b**).

Table 1

Name	CTRL	FTPC	FTIC	FSEIC	FTPC-obs
Correction area	None	Pacific Ocean coast to coast 25°S-25°N	Indian Ocean coast to coast 25°S-30°N	Indian Ocean 90°E to coast 0°S-10°S	Pacific Ocean coast to coast 25°S-25°N
Smoothing area	None	30°S-25°S 25°N-30°N	30°S-25°S	85°E-90°E, 115°E-120°E 15°S-10°S 0°-5°N	30°S-25°S 25°N-30°N
SST data	None	CTRL	CTRL	CTRL	OISSTv2
Time duration (Year)	210	110	110	60	50

Table 1: Summary of the numerical experiments with their main characteristics, including length, nudging domain and SST climatology used for the nudging in the Indian or Pacific oceans decoupled experiments. The nudged experiments are the Forced Tropical Pacific Climatology (FTPC) run, the Forced Tropical Indian Climatology (FTIC) run, the Forced South-East Indian Climatology (FSEIC) run and, finally, the Forced Tropical Pacific observed Climatology (FTPC-obs) run. See text for more details. For the FTPC and FTPC-obs experiments only ocean grid-points in the Pacific are included in the correction or smoothing areas and, similarly, for the FTIC and FSEIC experiments for their respective domains. The different correction domains are also displayed in Figure 1b-d. The observed SST climatology used in the FTPC-obs experiment is derived from the AVHRR only daily Optimum Interpolation SST version 2 (OISSTv2) dataset for the 1982–2010 period (Reynolds et al. 2007).

Click here to access/download
Electronic Supplementary Material
TableS1.doc
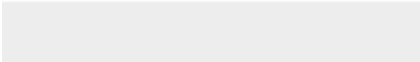
Click here to access/download
Electronic Supplementary Material
FigureS1_revised.eps